Specific Heat of the Dilute, Dipolar-Coupled, Ising Magnet $LiHo_xY_{1-x}F_4$

by

Jeffrey A. Quilliam

A thesis
presented to the University of Waterloo
in fulfillment of the
thesis requirement for the degree of
Master of Science
in
Physics

Waterloo, Ontario, Canada, 2006

I hereby declare that I am the sole author of this thesis. This is a true copy of the thesis, including any required final revisions, as accepted by my examiners.

I understand that my thesis may be made electronically available to the public.

Abstract

The system $LiHo_xY_{1-x}F_4$ is a nearly perfect example of a dilute, dipolar-coupled Ising magnet and, as such, it is an ideal testing ground for many theories in statistical mechanics. At low holmium concentration ($x = 0.045$) an unusual spin liquid or "anti-glass" state was discovered in previous work [1]. This state does not exhibit a spin glass freezing transition as is expected for a long-range interaction. Instead, it shows dynamics which are consistent with a collection of low-frequency oscillators [2]. It was also seen to have sharp features in its specific heat [3].

We present heat capacity measurements on three samples at and around the concentration of the spin liquid state in zero magnetic field and in a temperature range from around 50 mK to 1 K. In contrast to previous measurements, we find no sharp features in the specific heat. The specific heat is a broad feature which is qualitatively consistent with that of a spin glass. The residual entropy as a function of x, obtained through a numerical integral of the data, however, is consistent with numerical simulations which predict a disappearance of spin glass ordering below a critical concentration of dipoles [4].

Also presented here, is ac susceptibility data on an $x = 0.45$ sample which exhibits a paramagnetic to ferromagnetic transition and is found to be consistent with previous work.

Acknowledgements

First and foremost, I would like to thank my supervisor Jan Kycia. Jan is an incredibly creative and motivated scientist whose enthusiasm for experimental physics is unparalleled in my experience. During the three years I have spent working in his lab, he has provided priceless guidance, advice, motivation and the occasional pint of beer.

Michel Gingras has also been a very important guiding figure, providing theoretical support and the initial motivation for studying frustrated magnetism. He has been invaluable as a teacher and collaborator.

I would like to thank the other members of the group who, more than just co-workers, have become incredibly good friends of mine. Chas Mugford is exceedingly proficient in the lab and has provided so much good advice and assistance. Inevitably the low temperature physicist will develop at least two chemical dependencies – caffeine and liquid helium – and Nat Persaud, as the liquefier technician, has been my ever faithful source of the latter. Thanks to Lauren Lettress who was largely responsible for building the susceptometer used in this work and to Shuchao Meng for assistance with various projects in the lab.

Thanks to the members of the science machining group who have been a fantastic resource – especially Andy Coglough who has taught and continues to teach me the art of machining with seemingly infinite patience. Thanks to Rob Hill and Nina Heinig for frequent advice. Thanks to Graeme Luke, Sarah Dunsiger, Jose Rodriguez and Greg MacDougall for allowing me to participate in a μSR experiment and assisting with alignment of samples. Thanks to Stefan Kycia and Ariel Gomez for working on characterization of the crystals studied in this thesis.

Most importantly, thanks to my parents for their love and support and for helping me through so many challenging and expensive years of post-secondary education.

Contents

List of Tables

List of Figures

Chapter 1

Introduction

Most of the exotic systems that are currently researched in condensed matter physics are immensely complex. However, much of our theoretical understanding of these systems is based on simple toy models like the Hubbard model or the Ising model. Typically these are extreme simplifications of the actual physical systems that are studied experimentally, but even then they can be very difficult or impossible to solve.

The system $LiHo_xY_{1-x}F_4$ is a rare material which has almost as simple an underlying Hamiltonian as the toy models used in statistical physics and is thus an ideal testing ground for important theories in condensed matter physics. The low temperature physics of this material is dominated by the magnetic holmium (Ho^{3+}) ions. The crystal field anisotropy makes these ions nearly ideal Ising moments (only spin up or down) and they are coupled primarily by dipolar interactions. The Ho^{3+} ions may be diluted randomly by non-magnetic yttrium (Y^{3+}) ions with almost no change to the crystal structure. This allows one to study the effects of disorder in a well controlled fashion.

In previous work, the parent compound $LiHoF_4$ has been studied as a test of two diverse theories. First, renormalization group theory predicts that there is an upper critical dimension where there will be logarithmic corrections to the critical behaviour of a magnet. For most systems this dimension d^* is 4 or higher. For a dipolar-coupled magnet, however, d^* is 3 and so is accessible by experiment [5]. Second, it has also been studied as an example of the transverse field Ising model (TFIM) which exhibits a quantum phase transition in transverse magnetic field at zero temperature [6]. A 44% sample was studied to look at domain wall tunneling and glassy dynamics in a ferromagnet [7, 8] and a 16.7% compound was studied for the effects of transverse magnetic field on the spin glass state [9, 10].

Despite the apparent simplicity of this system's underlying model, however, there have been some surprising results. Possibly the most unusual of such effects, and the primary motivation for this work, is the appearance of a completely different magnetic phase at low

Ho^{3+} concentration (x). At $x = 0.045$, the system was found to have some very unusual dynamics that are completely unlike that of a spin glass [1] and it was dubbed an "anti-glass" state. This phase appeared to be a type of spin liquid in that it showed no indications of a transition to long-range order and so likely has only short-range correlations. It was also observed to exhibit nonlinear dynamics, coherent oscillations at low frequencies [2] and sharp features in the specific heat [3]. This unusual state has been proposed as a candidate for encoding quantum information because of its apparent macroscopic quantum behaviour [11]. This phase of the system is at odds with the classical expectation that an Ising magnet with long-range interactions should exhibit a transition to a broken symmetry or to spin glass order all the way to zero concentration of magnetic moments [12].

In this work, we have studied several stoichiometries in this series, largely in the vicinity of the 4.5% sample which was found to be so unusual. With a larger set of samples than have previously been measured, our aim is to refine the phase diagram of this system. We have performed ac susceptibility measurements in the ferromagnetic regime and specific heat measurements on low concentrations in the vicinity of the unusual "anti-glass" state at $x = 0.045$.

This thesis begins with a discussion of the Hamiltonian of $LiHo_xY_{1-x}F_4$ followed by a short overview of theory and experiments on spin glasses which are very important to the work presented here. Theory and numerical simulations of dilute Ising moments and the idea of a critical concentration below which spin glass order disappears are discussed in Chapter 4. An outline of the previous measurements that have been done on this same material and the broad spectrum of effects that have been observed are given in Chapter 5. Chapter 6 gives some calculations of the single-ion specific heat and in Chapters 7 and 8 we present our experimental methods and results respectively for both ac susceptibility and specific heat measurements.

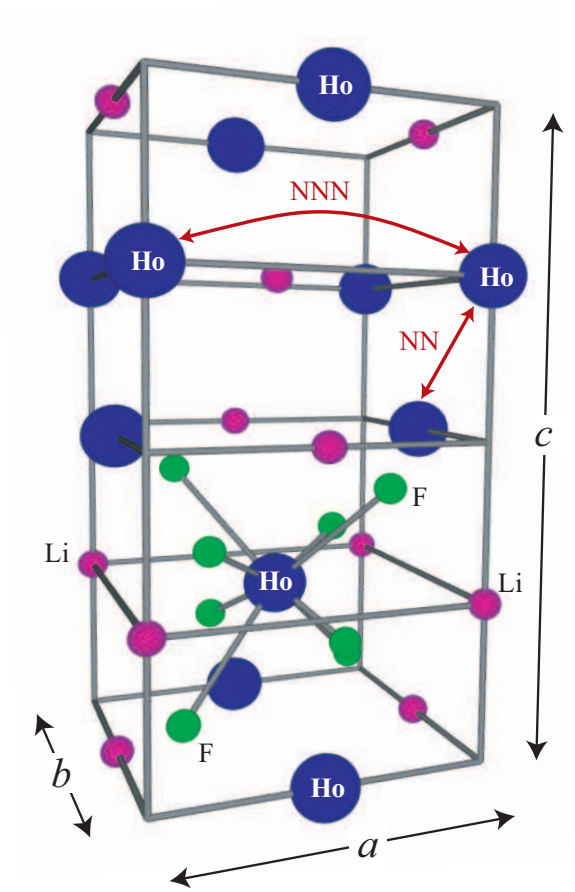

$$a = b = 5.176 \text{ Å}$$

$$c = 10.75 \text{ Å}$$

Figure 1.1: The crystal structure of $LiHoF_4$. It is a $CaWO_4$ lattice with space group $C^{6}{}_{4h}(I4_1/a)$ and with $a = b = 5.175$ Å and $c = 10.75$ Å [1]. The Ho^{3+} ions are shown in blue, the Li^+ ions in magenta and 8 of the F^- ions are shown in green (with others left out to simplify the diagram). The Ho ions may be replaced with Y ions during crystal growth with no discernable change in the crystal structure.

Chapter 2

The Hamiltonian of $LiHo_xY_{1-x}F_4$

The $4f$-valence electrons in Ho^{3+} have strong spin-orbit coupling so that they prefer to be in states of total angular momentum $J = 8$. This leaves 17 degenerate states for the free ion. In the crystal structure, however, the Ho ions are surrounded by F^- ions which create an electric potential or crystal field $\mathcal{H}_{\rm CF}$ with S_4 symmetry. Holmium is an isotopically pure element with nuclear spin $I = 7/2$. Since the $4f$-electrons are tightly bound about the nucleus and the holmium nucleus has a large magnetic moment, there is a significant hyperfine coupling of the form $A\mathbf{I}\cdot\mathbf{J}$ where $A \simeq 39$ mK.

There is a small nearest-neighbour exchange interaction $J_{\rm Ex}\mathbf{J}_i\cdot\mathbf{J}_j$, but the Ho moments are principally coupled by a long-range dipolar interaction

$$D_{ij}^{\alpha\beta}J_i^\alpha J_j^\beta = \frac{\mu_0}{4\pi}g_J^2\mu_B^2\left[\frac{\mathbf{J}_i\cdot\mathbf{J}_j}{r_{ij}^3} - \frac{3(\mathbf{J}_i\cdot\mathbf{r}_{ij})(\mathbf{J}_j\cdot\mathbf{r}_{ij})}{r_{ij}^5}\right]. \tag{2.1}$$

Of course, as with all magnetic systems, the application of a magnetic field is important, contributing an energy $g_J\mu_B\mathbf{B}\cdot\mathbf{J}$. The total magnetic Hamiltonian of $LiHo_xY_{1-x}F_4$ is therefore given by

$$\mathcal{H} = \mathcal{H}_{\rm CF} + J_{\rm Ex}\sum_{(i,j)}\mathbf{J}_i\cdot\mathbf{J}_j + \sum_{(i,j)}\sum_{\alpha\beta}D_{ij}^{\alpha\beta}J_i^\alpha J_j^\beta + A\sum_i\mathbf{I}_i\cdot\mathbf{J}_i - g_J\mu_B\sum_i\mathbf{B}\cdot\mathbf{J}_i. \tag{2.2}$$

We shall now analyze each of the terms in this Hamiltonian in some detail.

2.1 Crystal Field

The crystal structure of $LiHo_xY_{1-x}F_4$ has S_4 point-group symmetry. This means that it is invariant under a rotation of 90 degrees about the c-axis followed by reflection in the

ab-plane. The fluoride ions which surround the Ho ions create a strong electric potential or crystal field which interacts with the Ho^{3+} orbitals via Coulomb repulsion.

In rare-earth ions, the $4f$-electrons are tightly bound and the spin-orbit coupling $\lambda \mathbf{L}\cdot\mathbf{S}$ is typically larger than the crystal field energy. Thus the crystal field may be treated as a perturbation in the $|L, S, J, m_J\rangle$ basis. For transition metal ions, the spin-orbit interaction is often smaller than the crystal field so the correct basis to use is $|L, S, m_L, m_S\rangle$. For the rare-earth ion Ho^{3+}, $S = 2$ and $L = 6$ so the spin-orbit coupling gives $J = 8$ as the lowest energy multiplet with 17 degenerate m_J states. Different symmetries of crystal field will split the energies of these 17 states in different ways.

Assuming that the fluoride ions are close to point charges, the potential is given as

$$V(\mathbf{r}) = \sum_i \frac{q}{|\mathbf{R}_i - \mathbf{r}|} \tag{2.3}$$

which can be expanded as

$$V(r, \theta, \phi) = \sum_{n=0}^{\infty} \sum_{\alpha} r^n \gamma_{n\alpha} Z_{n\alpha}(\theta, \phi) \tag{2.4}$$

where

$$\gamma_{n\alpha} = \sum_i \frac{4\pi q}{(2n+1)} \frac{Z_{n\alpha}(\theta_i, \phi_i)}{R_i^{n+1}} \tag{2.5}$$

and the $Z_{n\alpha}$'s are the tesseral harmonics – spherical harmonics containing $\sin\phi$ or $\cos\phi$. To get the crystal field Hamiltonian, one must sum this energy over all of the valence electrons of the holmium (Ho^{3+}) moments so

$$\mathcal{H}_{\mathrm{CF}} = -e \sum_j V(\mathbf{r}_j). \tag{2.6}$$

This is best evaluated with Stevens' operator equivalents O_n^{α}, defined as

$$\sum_i r^n Z_{n\alpha}(x_i, y_i, z_i) \equiv c_{n\alpha} \theta_n \langle r^n \rangle O_n^{\alpha}. \tag{2.7}$$

$c_{n\alpha}$ is a constant which is part of $Z_{n\alpha}$. $\theta_2 = \alpha_J$, $\theta_4 = \beta_J$ and $\theta_6 = \gamma_J$ are the reduced matrix elements which depend on the angular momentum state of the ion in question. For Ho^{3+}, $\alpha_J = -1/(2 \cdot 3^2 \cdot 5^2)$, $\beta_J = -1/(2 \cdot 3 \cdot 5 \cdot 7 \cdot 11 \cdot 13)$ and $\gamma_J = -5/(3^3 \cdot 7 \cdot 11^2 \cdot 13^2)$ [13].

The crystal field Hamiltonian can then be expressed in terms of Steven's crystal field operators [14] as

$$\mathcal{H}_{CF} = B_2^0 O_2^0 + B_4^0 O_4^0 + B_4^{4C} O_4^{4C} + B_4^{4S} O_4^{4S} + B_6^0 O_6^0 + B_6^{4C} O_6^{4C} + B_6^{4S} O_6^{4S}. \tag{2.8}$$

The B_l^m coefficients are defined as

$$B_m^\alpha = -eq\theta_n\gamma_{n\alpha}c_{n\alpha}\langle r^n\rangle \tag{2.9}$$

These can be easily calculated except for q and the radial integral $\langle r^n\rangle$ which present more of a challenge and are often left as fitting parameters. Thus the symmetry of the potential determines which operators are not present, but the relevant crystal field parameters must be determined experimentally. This has been accomplished by choosing the parameters such that the resulting energy levels match with spectroscopic data. The relevant operator equivalents are given in terms of angular momentum operators (J_z, J_+, J_-, J^2) by

$$\begin{aligned}
O_2^0 &= 3J_z^2 - J^2 \\
O_4^0 &= 35Jz^4 - 30J^2J_z^2 + 25J_z^2 - 6J^2 + 3J^4 \\
O_4^{4C} &= \frac{1}{2}(J_+^4 + J_-^4) \\
O_4^{4S} &= \frac{i}{2}(J_+^4 - J_-^4) \\
O_6^0 &= 231J_z^6 - 315J^2J_z^4 + 735J_z^4 + 105J^4J_z^2 - 525J^2J_z^2 + 294J_z^2 - 5J^6 + 40J^4 - 60J^2 \\
O_6^{4C} &= \frac{1}{4}(J_+^4 + J_-^4)(11J_z^2 - J^2 - 38) + \text{H.c.} \\
O_6^{4S} &= \frac{1}{4i}(J_+^4 - J_-^4)(11J_z^2 - J^2 - 38) + \text{H.c.}
\end{aligned} \tag{2.10}$$

The experimentally determined crystal field parameters are given in Table 2.1. Several different sets of crystal field parameters have been determined from various spectroscopic data [15, 16, 17, 18, 19]. For this work we will use those taken from Chakraborty *et al.* [15]. Also listed in Table 2.1 are the crystal field parameters calculated here using the positions in Table 2.2 with the exception of q and the radial integrals. This calculation does allow one to estimate what certain ratios of parameters should be. For example the ratio B_4^{4c}/B_4^0 should be 7.78 if the F^- ions are close to point charges. The experimentally determined parameters do not agree with these ratios. For example, in Ref. [15] $B_4^{4c}/B_4^0 = 10.3$ which is different though at least in the same order of magnitude. This is likely because the point-charge model is quite a large assumption – the charges on the F^- ions come from the nuclei and the surrounding electrons thus the potential is probably quite far from $\sim 1/r$.

If the crystal field Hamiltonian is diagonalized on its own (treating the other terms in the Hamiltonian as perturbations), one obtains a ground state doublet

$$\begin{aligned}
|\uparrow\rangle &= 0.7945e^{i105^o}|7\rangle + 0.6052e^{-i68.6^o}|3\rangle + 0.0411e^{-i3.13^o}|-1\rangle - 0.0295|-5\rangle \\
|\downarrow\rangle &= 0.0295e^{i105^o}|5\rangle + 0.0411e^{-i71.8^o}|1\rangle + 0.6052e^{-i6.41^o}|-3\rangle - 0.7945|-7\rangle
\end{aligned} \tag{2.11}$$

Parameter	Ref. [15]	Calculated
B_2^0	-0.696 K	$-5.26 \times 10^{-5} eq\langle r^2 \rangle$
B_4^0	4.06×10^{-3} K	$9.68 \times 10^{-8} eq\langle r^4 \rangle$
B_4^{4C}	4.18×10^{-2} K	$7.53 \times 10^{-7} eq\langle r^4 \rangle$
B_4^{4S}	0 K	$-7.69 \times 10^{-7} eq\langle r^4 \rangle$
B_6^0	4.64×10^{-6} K	$1.42 \times 10^{-10} eq\langle r^6 \rangle$
B_6^{4C}	8.12×10^{-4} K	$1.24 \times 10^{-8} eq\langle r^6 \rangle$
B_6^{4S}	1.137×10^{-4} K	$-9.82 \times 10^{-9} eq\langle r^6 \rangle$

Table 2.1: Crystal Field parameters for $LiHo_xY_{1-x}F_4$ determined experimentally from spectroscopic data from Ref. [15]. Also listed are the crystal field parameters calculated with a point-charge model using the fluoride ion positions in Table 2.2 and Figure 2.1. The radial integrals are not easily calculable and the constant q is left as an overall fitting parameter in units of K/m^n. It is not clear why B_4^{4s} is missing in Ref. [15] and it may be best to reevaluate these crystal field parameters in future work.

F^- ion	R	θ	φ
1	2.246 Å	67.08°	33.00°
2	2.246 Å	112.92°	303.00°
3	2.246 Å	67.08°	213.00°
4	2.246 Å	112.92°	123.00°
5	2.293 Å	142.05°	36.98°
6	2.293 Å	37.95°	306.98°
7	2.293 Å	142.05°	216.98°
8	2.293 Å	37.95°	126.98°

Table 2.2: Positions of fluoride ions surrounding the Ho (or Y) ions. This distribution of ions has S_4 symmetry and gives rise to the crystal field anisotropy of the Ho moments.

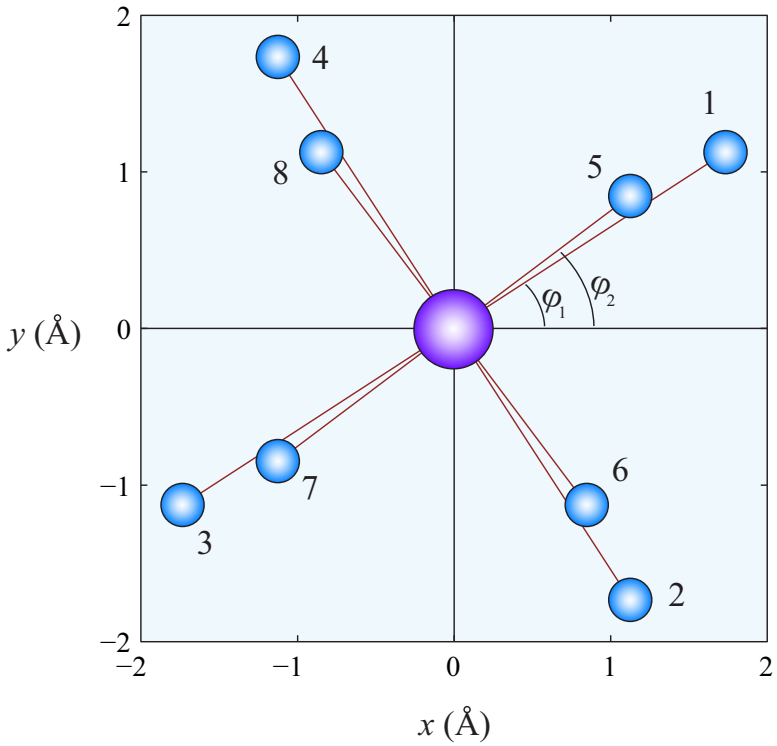

Figure 2.1: Positions of fluoride ions in the ab-plane surrounding the Ho ions at $(0, 0)$. $(R_1, \theta_1, \varphi_1) = (2.246\ \text{Å}, 67.08°, 33.00°)$ and $(R_2, \theta_2, \varphi_2) = (2.293\ \text{Å}, 142.05°, 36.98°)$ taken from Ref. [16]. The positions of all the fluoride ions are given in Table 2.2.

with the next excited state at ~ 11 K. Within this ground state doublet, all matrix elements of J_x and J_y are zero, and $\langle J_z \rangle = \pm 5.15$. This suggests that if the temperature is well below 11 K, the system is a near perfect Ising model with an effective g-factor

$$g_{eff} \equiv 2\langle J_z \rangle g_J = 13.8. \tag{2.12}$$

2.2 Nuclear Contribution

The holmium nucleus has an especially large magnetic moment of $4.173\mu_N$. Because of this and the fact that Ho^{3+} ions have $4f$ valence electrons which are tightly bound, the hyperfine interaction is very important. This interaction takes the form

$$\mathcal{H}_i^{HF} = A\mathbf{I}_i \cdot \mathbf{J}_i \tag{2.13}$$

and leads to a splitting of the electronic energy levels into 8 energies corresponding to the m_I values of the $I = 7/2$ nuclear spin.

Various values for A have been determined experimentally. One method used to determine this constant is electron paramagnetic (or spin) resonance (EPR/ESR). Resonances are found when the Zeeman energy $\mu_B g_J \mathbf{B} \cdot \mathbf{J}$ is equal to the energy of other interactions in the system. For every crystal field level, there are therefore 8 resonances associated with the 8 nuclear levels. The field splitting between these resonances can then give the energy of the nuclear hyperfine interaction:

$$A = \mu_B g_J \Delta B \tag{2.14}$$

The Landé g-factor for Ho^{3+} is 5/4. For a free Ho^{3+} ion, EPR experiments find $A/k_B = 38.975$ mK [20]. For a Ho^{3+} ion in the $LiHoF_4$ lattice, EPR experiments find $A/k_B = 39.799$ mK [21] and for dilute ions in the $LiYF_4$ lattice, $A/k_B = 40.210$ mK [22]. Calculations here will use the latter value $A/k_B = 40.210$ mK as the lattice is most similar to that studied in this work.

Also important to consider is the nuclear quadrupole interaction with the electric field gradient at the nucleus. This interaction is described [20] by

$$\mathcal{H}^Q = \frac{Q}{4I(2I-1)}\left[3I_z^2 - I^2 + \frac{\eta}{2}(I_+^2 + I_-^2)\right] \tag{2.15}$$

where

$$\eta = \frac{V_{xx} - V_{yy}}{V_{zz}} \quad \text{and} \quad V_{\alpha\beta} = \frac{\partial^2 V}{\partial\alpha\partial\beta}. \tag{2.16}$$

Many of the parameters involved are difficult to calculate and we will just replace them with a single experimentally-determined parameter P. The nuclear moments will be strongly coupled to the up or down Ising spins so it is likely that the off-diagonal x and y components will have a small effect. Thus we will assume η to be 0 as is often done [23]. The quadrupolar interaction then becomes

$$\mathcal{H}^Q = PI_z^2 \tag{2.17}$$

plus a constant term. The value of P determined by EPR is only 1.7 mK [23], but since this term is dependent on the square of I_z, it is still significant with respect to the hyperfine interaction energy and will be just noticeable in calculations of the specific heat.

2.3 Dipolar Coupling

In $LiHo_xY_{1-x}F_4$ there is a small nearest-neighbour antiferromagnetic exchange interaction

$$J_{\text{Ex}}\mathbf{J}_i \cdot \mathbf{J}_j \tag{2.18}$$

where $J_{\text{Ex}}/k_B \simeq 0.16$ K [15]. The Ho^{3+} ions, however, are primarily coupled via a weak dipolar interaction

$$\mathcal{H}_{ij}^{\text{Dipolar}} = \sum_{\alpha\beta} D_{ij}^{\alpha\beta} J_i^\alpha J_j^\beta = \frac{\mu_0}{4\pi} g_J^2 \mu_B^2 \left[\frac{\mathbf{J}_i \cdot \mathbf{J}_j}{r_{ij}^3} - \frac{3(\mathbf{J}_i \cdot \mathbf{r}_{ij})(\mathbf{J}_j \cdot \mathbf{r}_{ij})}{r_{ij}^5} \right]. \tag{2.19}$$

If the moments are taken to be perfect Ising moments along the z-direction then this interaction simply becomes

$$\mathcal{H}_{ij}^{\text{Dipolar}} = \frac{\mu_0}{4\pi} g_{\text{eff}}^2 \mu_B^2 \left(\frac{r_{ij}^2 - 3z_{ij}^2}{r_{ij}^5} \right) S_i^z S_j^z \tag{2.20}$$

where the S_i^z are spin 1/2 operators. It is important to note that the dipolar interaction is angle-dependent. If the vector connecting two spins is close to the z- or c-axis, the interaction is ferromagnetic. If the spins are closer to within the ab-plane, however, the interaction will be antiferromagnetic. This leads to a degree of frustration in the system. For the nearest neighbours in this system the dipolar interaction is ferromagnetic with an energy $E_{\text{NN}} = \pm 318$ mK. The next nearest neighbours, on the other hand, have an antiferromagnetic interaction of strength $E_{\text{NNN}} = \pm 214$ mK. The nearest neighbour (NN) and next-nearest neighbour (NNN) sites are shown on the crystal structure in Figure 1.1.

2.4 Transverse Magnetic Field

The addition of any external magnetic field introduces a term, the Zeeman energy, to the Hamiltonian of the form $g_J\mu_B\mathbf{B}\cdot\mathbf{J}$. Most interesting, is the introduction of a transverse field B_x. Such a field leads to mixing of the ground states of the crystal field via the next excited state. Thus with increasing transverse field the Ising character of the moments is reduced and quantum fluctuations are allowed to occur more easily.

The coupling with the next excited state can be expressed as a term ΓS^x in the effective spin-1/2 Hamiltonian where Γ is the effective transverse field (as opposed to the real transverse field $B_\perp$) [15]. With the addition of this term, Equation (2.20) becomes the dipolar transverse field Ising model (TFIM):

$$\mathcal{H} = J_0 \sum_{\langle ij \rangle} \left(\frac{r_{ij}^2 - 3z_{ij}^2}{r_{ij}^5} \right) S_i^z S_j^z - \Gamma \sum_i S_i^z. \tag{2.21}$$

The transverse field Ising model is one of the simplest models that exhibits a quantum phase transition. A quantum phase transition is a zero-temperature transition that occurs as some parameter of the Hamiltonian is adjusted, be it the dilution x, pressure P or magnetic field B. In this case the parameter which is being tuned is the transverse magnetic field Γ. Before the introduction of Γ, the Hamiltonian was diagonal in the $|\uparrow\rangle_i$,$|\downarrow\rangle_i$ basis. The transverse field, however, is an off-diagonal term ($\hat{S}^z$ and $\hat{S}^x$ do not commute). This allows tunneling events between the up and down Ising states or quantum fluctuations.

The quantum phase transition results from non-analytical behaviour of the ground state energy at a critical value of the parameter Γ, or at Γ_c [24]. For very low Γ and T the system is ordered ferromagnetically, but for very large Γ it is a quantum paramagnet as the dipolar coupling is weak compared to the transverse field term. In the ferromagnetic phase, the magnetization is gradually reduced by increasing Γ as quantum fluctuations allow spins to flip. At the transition Γ_c, the quantum fluctuations completely destroy the ferromagnetic order so that the magnetization is 0, just as thermal fluctuations destroy order in a classical phase transition. For $\Gamma > \Gamma_c$ the system has an exponentially decaying correlation function $\langle S_i^z S_j^z \rangle \sim e^{-|x_i - x_j|/\xi}$ where ξ is the correlation length. As Γ is lowered towards Γ_c, this correlation length gets larger and diverges at the transition.

Quantum phase transitions in d dimensions may generally be mapped onto classical phase transitions in $d+1$ dimensions. Thus the quantum phase transition in the 3-dimensional dipolar TFIM is equivalent to the classical phase transition in the 4-dimensional dipolar Ising model. Experiments that studied the quantum phase transition in $LiHoF_4$ [6] and looked for a quantum phase transition in the Ising spin glass $LiHo_{0.167}Y_{0.833}F_4$ [9, 10] will be discussed in detail in Chapter 5.

Chapter 3

Spin Glasses

The two main ingredients for a spin glass state are frustration and randomness. Frustration arises from competing interactions so that it is difficult to find a spin configuration with a minimum energy. Such frustration can result from a number of different interactions including the dipolar coupling which applies to the system being studied here. There are many examples of frustrated spin systems which do not form spin glass states, for example the spin ice materials $Dy_2Ti_2O_7$ and $Ho_2Ti_2O_7$ [25, 26]. Though there is some evidence that the frustrated magnet $Gd_3Ga_5O_{12}$ develops a spin glass state despite having very little disorder [27], generally speaking spin glasses only result from a high degree of randomness either in the position of the spins or in the strength of the interactions.

A spin glass state is characterized by a freezing of the magnetic moments into a disordered state. Clearly this is analogous to a real, structural glass which is a solid (frozen) but does not develop any crystal structure or long-range order. There is a multitude of "glassy" systems which appear to remain disordered down to low temperatures, but one of the important questions has long been whether these materials undergo a second-order phase transition (glass transition) to a frozen state or whether it is a continuous freezing of the moments. The general consensus now, is that some of these glassy systems do indeed undergo a sharp spin glass transition at a temperature T_g [28].

3.1 Experimental Evidence

The first indication of the existence of a spin glass state was a linear specific heat measured at low temperatures in the alloys CuMn and AuFe which could not be explained in magnitude by the conduction electrons [29]. It was realized that the specific heat was coming from the Mn or Fe Ising moments interacting via the RKKY interaction (described

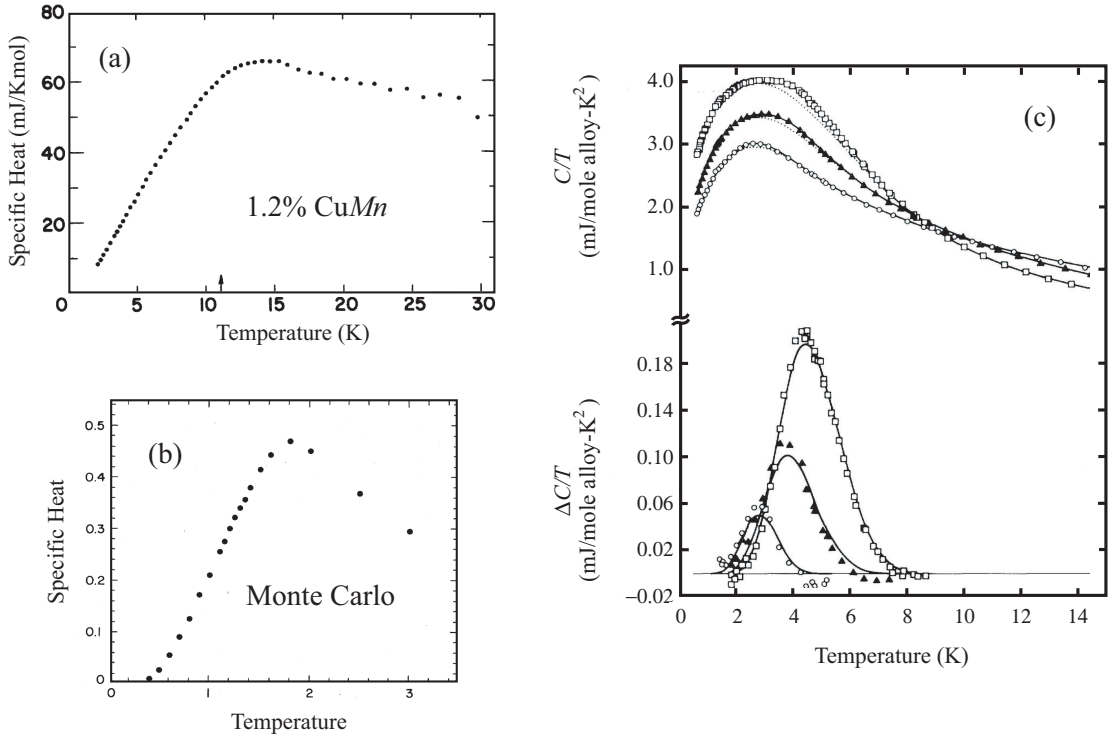

Figure 3.1: (a) The specific heat of the spin glass Cu*Mn* at 1.2% Mn from Ref. [31] and (b) the specific heat of a spin glass computed by Monte Carlo simulation [32]. (c) Measurements of Fogle *et al.* [33] of the specific heat of Cu*Mn*. The lower curves, ΔC are an anomaly at the spin glass transition temperature found from fitting spline curves to C and taking derivatives with respect to temperature.

in Section 3.2) which is somewhat random. Anderson *et al.* proposed that the linear dependence of the specific heat at low temperatures was coming from a collection of two-level systems (TLS's) with a distribution of energies and therefore tunneling rates [30]. Ising moments effected by a distribution of effective magnetic fields are a prime example of two-level systems. TLS's of a different sort are also seen in real, structural glasses.

If the specific heat is measured over a wider range of temperatures, it is seen to be a broad feature with no sharp anomalies (see for example References [31, 34, 35] and Figure 3.1(a)). This seemed to be a strong indicator that there was no sharp transition. Since then, however, mean-field theories of spin glasses have predicted that the critical exponent α is very negative, in the range -2 to -4, thus there should be next to no indication

of a transition in the specific heat C [28]. Fogle *et al.* did very careful measurements of the specific heat (shown in Figure 3.1(c)), fit spline curves and took derivatives with respect to temperature and were able to see a slight feature in the vicinity of the spin glass freezing transition [33].

In support of the idea that a spin glass has a sharp transition are measurements of the susceptibility as a function of temperature. These measurements observe a fairly sharp cusp and then a drop in the susceptibility as the local spontaneous magnetization reduces the susceptibility (as happens in a ferromagnet for example) [36, 37]. What is unusual about the susceptibility is that it was found to be very dependent on the frequency at which it is measured [38]. The cusp appears at a temperature $T_f(\omega)$, and moves to lower temperatures as the frequency is lowered as is shown in Figure 3.2(a). This cusp is also found to be slightly rounded, even for very small excitation fields [39, 40].

The precise behaviour of $T_f(\omega)$ varies between specific spin glasses. In some cases [1], it appears to obey an Arrhenius law

$$\frac{\omega}{\omega_0} = \exp\left[-\frac{E_a}{k_B T_f(\omega)}\right]. \tag{3.1}$$

In other cases [41], if one measures to low enough frequencies, the ac susceptibility appears to obey a Fulcher law

$$\frac{\omega}{\omega_0} = \exp\left[-\frac{E_a}{k_B(T_f(\omega) - T_0)}\right] \tag{3.2}$$

with a finite dc limit of the freezing temperature as is shown in Figure 3.2(b). One may be tempted to take T_0 as the glass temperature T_g. However, to be consistent with Monte Carlo simulations, a so-called dynamical scaling analysis should be used to determine the spin glass freezing transition.

$$\frac{\tau(T)}{\tau_0} = \left(\frac{T - T_g}{T_g}\right)^{-z\nu} \tag{3.3}$$

where $z\nu$ is a critical exponent. In Monte Carlo simulations $z\nu$ is found to be ~ 7.0 [32]. There are various ways that τ can be defined. For instance it can be defined as the inverse frequency at which $\chi''(\omega)$ is a maximum or it is sometimes [1] defined as

$$\lim_{\omega \to 0} \frac{\chi''(\omega)}{\omega \chi'(\omega)} \tag{3.4}$$

Spin glasses also exhibit significant remanence effects in their magnetization and susceptibility below T_g. Very different values of the static susceptibility will be measured if the sample is field cooled or zero-field cooled even for very small magnetic fields [43]. The

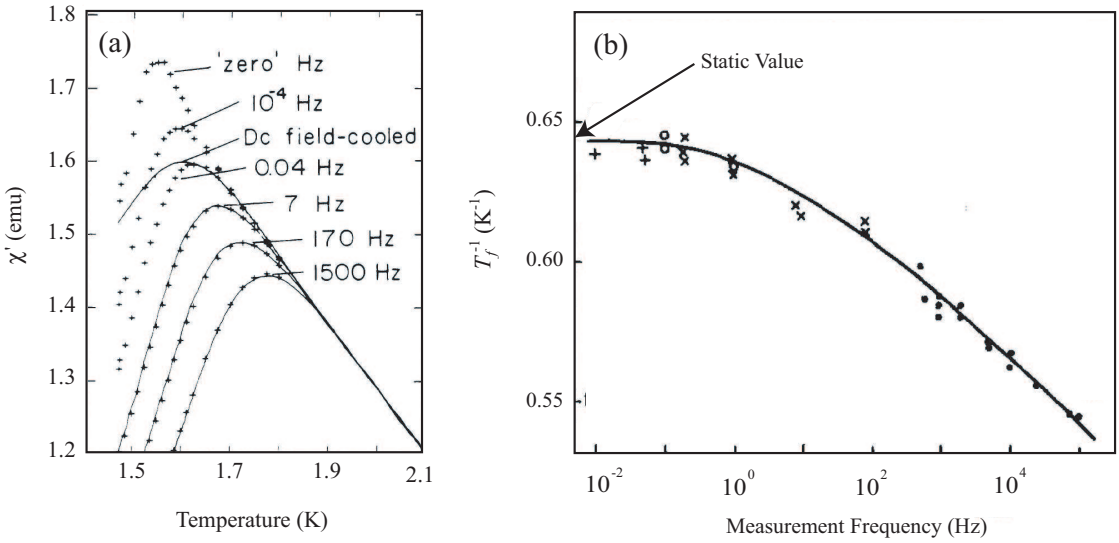

Figure 3.2: (a) The ac susceptibility of $Eu_{0.4}Sr_{0.6}S$ for different measuring frequencies [42]. The cusp $T_f(\omega)$ is seen to move to lower temperatures as the measuring frequency is lowered. (b) The inverse freezing temperature T_f^{-1} plotted as a function of measuring frequency (obtained from several different measurement techniques) [41]. The freezing temperature tends towards a finite static value.

remanent magnetization is found to be time dependent so that if the field is turned off, the magnetization will very slowly decay to 0, often with slower than exponential relaxation, for example as $M_R(t) \propto \exp[-(t/\tau)^{\beta}]$ [41].

Possibly one of the most convincing arguments for the existence of a spin glass transition is the apparent divergence of the non-linear susceptibility at T_g. The non-linear susceptibility or χ_{nl} is defined as follows. If the magnetization is measured as a function of magnetic field, one obtains not only a linear term, but also a cubic and higher order terms:

$$\chi = M(H)/H = \chi_0(T) - H^2\chi_{nl}(T) + \mathcal{O}(H^4). \tag{3.5}$$

Fits to $M(H)$ give a value for χ_{nl} which has been seen in many systems (see for example Monod and Bouchiat [44]) to diverge as

$$\chi_{nl}(T) \propto \left(\frac{T - T_g}{T_g}\right)^{\gamma} \tag{3.6}$$

where γ most often takes a value $3 < \gamma < 4$ [45].

There is a large set of experimental techniques and methods of data analysis for determining spin glass freezing temperatures, only a few of which I have listed above.

3.2 Models and Order Parameters

The first spin glasses to be studied were alloys of magnetic transition metal impurities with noble metal hosts like Cu*Mn* and Au*Fe* [28]. In these systems, the magnetic impurities are coupled via the Ruderman-Kittel-Kasuya-Yosida (RKKY) interaction. The magnetic impurities polarize the surrounding conduction electrons. This polarization decays as $1/r^3$ while oscillating about 0 at a wavevector $2k_F$ where k_F is the Fermi wavevector. Then, nearby impurities feel the effect of this polarization, hence there is coupling between the moments. Since the polarization is oscillating spatially, the coupling between two randomly positioned impurities is random, and may be positive or negative, resulting in competing interactions.

Slightly more recently, the magnet $Eu_xSr_{1-x}S$ was discovered to behave as a spin glass for certain values of x. This material has ferromagnetic nearest neighbour exchange interactions and antiferromagnetic next-nearest neighbour exchange interactions. It is a ferromagnet for $x = 1$, but if the Eu moments are sufficiently diluted, there is randomness and frustration and it becomes a spin glass. The fact that this very different type of magnet also demonstrates spin glass behaviour indicates that there is some degree of universality about spin glasses and that simple toy models might be used to understand them [28].

The Edwards-Anderson (EA) model is one such toy model. It consists of a lattice of spins $\mathbf{S}_i$, each of which is coupled to every other spin $\mathbf{S}_j$ by a random interaction strength J_{ij}. The distribution of coupling strengths is a Gaussian distribution, centred about 0, with a variance $\sigma^2 = \Delta_{ij} = \Delta(\mathbf{R}_i - \mathbf{R}_j)$ which is a function of the distance between the spins [46]. Often, the moments are taken to be Ising spins so that only S_i^z enters the Hamiltonian.

The Sherrington-Kirkpatrick (SK) model is a simplification of the EA model, where Δ_{ij} is no longer a function of the distance between spins. Thus, it is an infinite-range model. A lattice is no longer necessary because we simply have N spins, each of which is coupled randomly to every other spin [47].

In standard phase transitions, a symmetry is broken at the critical temperature. For example in an Ising ferromagnet, above the transition temperature, the system is disordered and the spins may orient in any direction. Below the critical temperature, however, the spins in the system are expected to be either all up or all down. Clearly both of these states have the same energy, but it is impossible for the entire system to switch back and forth between them. To explain this theoretically, one starts with an infinitesimally small field h in one of those directions which is allowed to go to zero after taking the thermodynamic limit $N \to \infty$.

In a spin glass, things are not so simple. There is no obvious symmetry broken as the temperature is lowered. Instead, the spins freeze into a disordered state. There may in fact be many stable minima in the free energy surface each corresponding to a different, disordered configuration of the moments.

There are several different order parameters which may be chosen for a spin glass. Clearly the magnetization m is not appropriate as the spins are expected to be disordered. The most obvious choice would be the mean square magnetization

$$q = \left[\langle S_i \rangle^2\right]_{\text{av}}. \tag{3.7}$$

The $[\ \ ]_{\text{av}}$ is an average over the disorder in the system where as the $\langle\ \ \rangle$ is a thermal average. q is known as the equilibrium or statistical mechanics order parameter. It is often used in theoretical models even if it is not necessarily appropriate in experiment as it can be very difficult, or even impossible, to obtain equilibrium data.

A more realistic order parameter is the Edwards-Anderson (EA) order parameter [46]. It is defined dynamically as

$$q_{EA} = \lim_{t\to\infty} \lim_{N\to\infty} \left[\langle S_i(t_0) S_i(t_0 + t)\rangle\right]_{\text{av}} \tag{3.8}$$

In this case, averaging over different reference times t_0 can be seen as equivalent to averaging over the disorder in the system. If the system is ergodic (accesses all states) this will be

zero, but if it is trapped in a single phase (a local minimum of the free energy) then it will be non-zero and there will be 'broken ergodicity'. Only an infinite system can get completely 'stuck' in such a phase – a finite system will always, eventually find its way into the true equilibrium state [28].

Often spin glasses are described as having a very complicated free energy 'landscape' with many stable minima or 'valleys' and barriers separating those valleys. Below the freezing transition, the barriers separating the different phases of the system may be infinitely high and the system cannot switch between them. If the index a is used to denote the different valleys of the free energy landscape then

$$q_{EA} = \left[\sum_a P_a (m_i^a)^2 \right]_{\text{av}} \tag{3.9}$$

where $P_a \propto \exp(-\beta F_a)$. The equilibrium order parameter on the other hand is given as

$$q = \left[\left(\sum_a P_a m_i^a \right)^2 \right]_{\text{av}} \tag{3.10}$$

thus there are terms coming from mixing of the valleys. In reality, neither of these order parameters is entirely relevant. Instead, it is expected that one or the other may apply depending on the time scales involved. If an experiment is carried out quickly, there is not sufficient time for the system to reach equilibrium and q_{EA} should be appropriate. But if one waits long enough, it is expected that the system would eventually reach equilibrium and q would be appropriate as an order parameter [28].

3.3 The Replica Method

A frequent problem in the study of spin glasses is how to average over the disorder in the problem. This is often handled by the 'replica method' or 'replica trick' [28]. When calculating physical quantities, one wishes to average the log of the partition function $\ln \mathcal{Z}$ over the disorder which is generally very difficult. The replica trick makes this easier by the identity

$$\ln \mathcal{Z} = \lim_{n \to 0} \frac{\mathcal{Z}^n - 1}{n}. \tag{3.11}$$

Now one can start by working with n replicas of the partition function

$$\mathcal{Z}^n = \prod_{\alpha=1}^{n} \mathcal{Z} = \text{Tr} \exp \left(-\beta \sum_{\alpha=1}^{n} \mathcal{H}\{S_i^\alpha\} \right) \tag{3.12}$$

then averaging over the disorder

$$[\mathcal{Z}^n]_{\rm av} \equiv {\rm Tr}\exp(-\beta\mathcal{H}_{\rm eff}) \tag{3.13}$$

and later take the limit as $n \to 0$ [28]. This technique is used frequently in the study of various spin glass models. It can, however, result in some complications stemming from the order in which various limits ($N \to \infty$, $n \to 0$, etc.) are taken [45].

In terms of the replica method, the order parameter q can be defined as

$$q = \lim_{n\to 0} \frac{1}{n(1-n)} \sum_{\alpha\neq\beta} q^{\alpha\beta} \tag{3.14}$$

where

$$q^{\alpha\beta} = N^{-1} \sum_i \langle S_i^\alpha S_i^\beta \rangle = N^{-1} \sum_i {\rm Tr} S_i^\alpha S_i^\beta \exp(-\beta\mathcal{H}_{\rm eff}). \tag{3.15}$$

The first attempts at a mean-field theory of spin glasses used the replica method and the SK model and assumed that the results should be 'replica symmetric' – in other words that $q^{\alpha\beta}$ should be the same for all α and β [47]. This gave some unphysical results, including a negative entropy [28]. It was found that one needed to break replica symmetry in order to obtain the correct mean-field solution [48, 49]. This broken replica symmetry is closely connected to broken ergodicity and the Edwards-Anderson order parameter [28]. This replica method will be used briefly in the next chapter to understand the effect of dilution on dipolar-coupled Ising moments.

Chapter 4

Phase Diagram of Dilute, Ising Moments

In this chapter, we will discuss the theoretically expected phase diagram of diluted Ising moments. At high concentrations of magnetic moments (x) a symmetry breaking transition is usually expected. This might be antiferromagnetic or ferromagnetic depending on the interactions, the lattice and anisotropy in the moments.

In some cases, at lower concentrations, the system can become a spin glass. In short range systems there is a percolation threshold x_c below which point there is no longer any finite ordering transition temperature. In long-range systems, however, there cannot be a percolation threshold. It has long been thought, therefore, that there should be no critical concentration below which the ordering transition disappears in a dipolar-coupled system [12]. As will be discussed in detail in Section 5.4, the system $LiHo_xY_{1-x}F_4$ has been seen to have a lack of ordering transition below a certain concentration x. Recent Monte Carlo experiments also suggest that there is no spin glass transition below a certain value of x in dipolar-coupled Ising systems [4].

4.1 Percolation Threshold

If one starts with an empty lattice ($x = 0$) and gradually increases x, one expects that the mean size of clusters (within which all ions are connected by short-range interactions) to increase. In an infinite system there is a point x_c at which the mean cluster size will diverge. This point is known as the percolation threshold. Formally, x_c is defined as the largest value of x for which any given site definitely (with probability 1) belongs to only a finite cluster. For $x > x_c$ there is a non-zero probability $P(x)$ that a given ion belongs to

a cluster of unbounded size.

The term 'percolation' comes from fluid flowing through a porous material. If the density of the material is sufficient, the spaces or pores will all be isolated from one another and liquid will not be able to flow. There can be a critical density, however, below which there is a cluster of connected pores the size of the system itself. At this point, a liquid would be able to percolate through the material.

The percolation problem may be formulated as a site-dilution problem (removing ions) or as a bond-dilution problem (removing interactions between moments) giving different results [50]. Various lattices and types of interactions yield different percolation thresholds. For the site-diluted problem on the triangular lattice with nearest neighbours only, $x_c = 0.5$ [50]. This is one of the few cases that can be calculated exactly but there are numerical methods which are expected to be close to the exact value. For a square lattice, for example, $x_c = 0.59 \pm 0.01$ (according to calculations) [50].

In 3-dimensional lattices the percolation threshold is generally lower. For example the simple cubic lattice has $x_c \simeq 0.307$, the body-centred cubic lattice has $x_c \simeq 0.243$ and the face-centred cubic lattice has $x_c \simeq 0.195$ (all for nearest neighbours only). Including further neighbour interactions also reduces x_c as much fewer filled sites are required to form an infinite percolating cluster.

Now we must ask how the dilution can theoretically effect the magnetic ordering of a given sample. A transition depends on the limit of infinite cluster size. This way the energetically equivalent ground states ($\langle m \rangle = \pm 1$ in a ferromagnet) are separated by an energy barrier of infinite size and an infinitesimally small magnetic field h will push the system into one or the other. If there are many clusters of finite size in the system, however, the energy barriers will not be infinite in the thermodynamic limit and there will be no symmetry-breaking transition [50]. Thus for Ising moments in 2 or higher dimensions, there will be a transition for $x > x_c$ but there will be no transition for $x < x_c$.

It is also expected that there will be a change in critical behaviour as a function of the concentration of magnetic moments in the system above x_c [51]. In fact the dilution can completely alter the type of transition, resulting in a spin glass state [52].

4.2 Dilute, Dipolar-Coupled Moments

For a long-range interaction such as the dipole interaction, there should not be any finite concentration of moments at which there are decoupled clusters, thus there is no percolation threshold. In this section we will discuss the mean-field theory of Stephen and Aharony [12]. This provides us with some expectation of what the transition temperature will be as a function of the concentration of moments in a dipolar-coupled Ising magnet.

To study this system, we start with n replicas of the Ising model averaged over the bond distribution (which in this case is J_{ij} with probability x and 0 with probability $1-x$).

$$[\mathcal{Z}^n]_{\text{av}} = \text{Tr} \prod_{ij} \left[1 + \nu \exp\left(\beta J_{ij} \sum_{\alpha=1}^{n} S_i^\alpha S_j^\alpha \right) \right] \equiv \text{Tr} \exp(-\beta \mathcal{H}_{\text{eff}}) \tag{4.1}$$

where $\nu = x/(1-x)$ [51]. The effective Hamiltonian can be written as an expansion in higher-order spin interactions between the different replica indices.

$$\mathcal{H}_{\text{eff}} = \sum_{ij} \sum_{l=1}^{n} K_{ij}^l Q_{ij}^l \tag{4.2}$$

where

$$Q_{ij}^1 = \sum_{\alpha=1}^{n} S_i^\alpha S_j^\alpha, \quad Q_{ij}^2 = \sum_{\alpha<\beta} S_i^\alpha S_j^\alpha S_i^\beta S_j^\beta, \quad \text{etc.} \tag{4.3}$$

The K_{ij}^l's are expansion coefficients which depend on x, T and the J_{ij}'s.

Thus the effective Hamiltonian contains the competing order parameters: $\mu_i^\alpha = \langle S_i^\alpha \rangle$, $\mu_i^{\alpha\beta} = \langle S_i^\alpha S_i^\beta \rangle$, etc. whose Fourier transforms are σ_q^α, $\sigma_q^{\alpha\beta}$, etc. The first of such order parameters μ_i^α is simply the magnetization m_i and is thus the order parameter appropriate for a ferromagnet. The next $\mu_i^{\alpha\beta} = q_i^{\alpha\beta}$ is a candidate for the spin glass order parameter. Fourier transforming the effective Hamiltonian gives

$$\mathcal{H}_{\text{eff}} = -\frac{1}{2} \sum_l \sum_q (\hat{K}_q^l - 1) |\sigma_q^{\alpha_1 \ldots \alpha_l}|^2 + \mathcal{O}(\sigma^3) \tag{4.4}$$

The critical temperature at which ordering will take place is found by

$$r_l = 1 - \hat{K}_0^l = 0 \tag{4.5}$$

To leading order,

$$K_{ij}^l \simeq x[\tanh(\beta J_{ij})]^l. \tag{4.6}$$

Thus for the ferromagnetic order parameter μ_i^α, the transition line will be given approximately by

$$r_1 = 1 - x \sum_j \tanh(\beta J_{ij}) = 0 \tag{4.7}$$

If the expansion is carried out more rigorously, however,

$$r_1 = 1 - x\beta\varphi' \tag{4.8}$$

where

$$\varphi' = \varphi + \frac{k_B T}{J_0} \sum_j \left[\tanh\left(\frac{J_{ij}}{k_B T}\right) - \frac{J_{ij}}{k_B T} \right] \tag{4.9}$$

and where $J_0\varphi$ is the low-momentum limit of the Fourier transform of the dipolar interaction [53]. The quantity φ depends on the lattice involved and was calculated for the $LiHo_xY_{1-x}F_4$ lattice by Fujiki *et al.* [54]. At high concentrations $r_1 < r_2$ and the system will order ferromagnetically at transition temperatures which approach a straight line given by $k_B T_C(x) \propto x \sum_j J_{ij}$.

In some cases φ' can be quite small. Then it is possible that $r_2 < r_1$ at lower concentrations (x) [12]. This would imply that the order parameter $\mu_i^{\alpha\beta}$ would order first and the ferromagnetic order would be replaced by spin glass order at a temperature T_g found by

$$r_2 = 1 - x \sum_j [\tanh(\beta J_{ij})]^2 = 0. \tag{4.10}$$

This appears to be the case for the $LiHo_xY_{1-x}F_4$ below $x \simeq 0.25$ both in the calculation (see Figure 4.1) and in experiment [1]. In either case, a percolation threshold x_C is not expected for this model as $T_C(x)$ only goes to zero as $x \to 0$ [12].

4.3 Monte-Carlo Simulations

The very recent work of Snider and Yu [4] suggests that there is a lack of ordering at low concentrations of Ising dipoles. They performed Wang-Landau Monte Carlo simulations of dilute Ising spins on a simple-cubic lattice for various concentrations x and system sizes $N = L^3$. A generalized Edwards-Anderson order parameter q is defined as the overlap of the state of the system S_i^s with a common low-energy state S_i^q. They start with an initial guess and then proceed with a random walk in configuration space. While this is done, the energy E of the system and the order parameter q are tallied. If enough parameter space is visited, the density of states $n(E)$ and probability of occupation of the order parameter and energy $F(q, E)$ may be evaluated. Then for a given temperature T

$$P(q) \propto \sum_E n(E) F(q, E) e^{-E/k_B T}. \tag{4.11}$$

It is the evolution of the shape of $P(q)$ as a function of temperature which is used to determine whether the system is ordering as a spin glass or not. It is expected, for a spin glass, that $P(q)$ should be Gaussian in q at high temperatures and below the freezing temperature it should be bimodal at $q = \pm 1$. The freezing temperature, for a given system

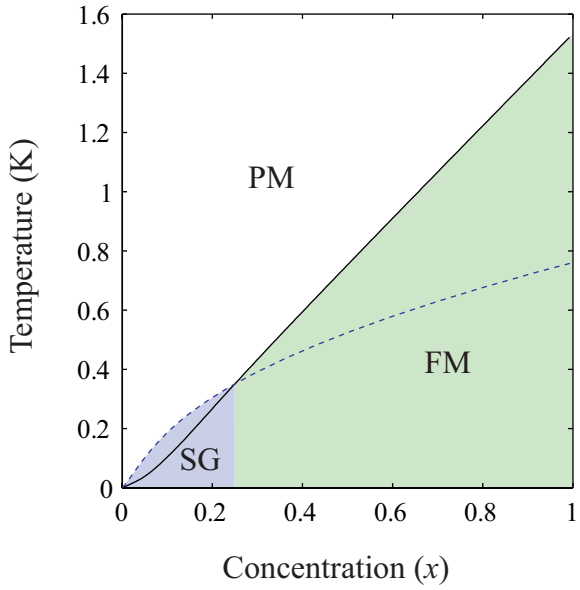

Figure 4.1: The calculated phase diagram of dilute dipolar-coupled Ising moments on the $LiHo_xY_{1-x}F_4$ lattice using the theory of Stephen and Aharony [12]. The solid black line is for the ferromagnetic order parameter μ_i^α from Equation (4.7) and the dashed blue line is for the spin glass order parameter $\mu_i^{\alpha\beta}$ given by Equation (4.10). The interactions in the system have been scaled to give $T_c(x = 1) = 1.53$ K.

size, can be defined as some point in between these two extremes where $P(q)$ is flattest. This results in a freezing temperature T_f which is decreasing with system size. Thus in some sense, the system size is analogous to the time scale in a physical measurement. For $x = 0.045$, $x = 0.12$ and $x = 0.20$, this freezing temperature seems to extrapolate to 0 in the limit of infinite system size, indicating that there is no finite spin glass transition temperature.

Snider and Yu also calculate the entropy of the systems as a function of temperature. It is a smooth function which indicates a broad, smooth bump in the specific heat. At a critical concentration of moments $x_c = 0.2$, there is no residual entropy, but at lower concentrations S_0 becomes noticeable with it reaching around $8 \times 10^{-3} k_B$ per particle at 4.5% (see Figure 4.2). This residual entropy would seem to result from a flat energy landscape with many accessible and nearly degenerate ground states. In a spin glass, the energy barriers should be higher, so the spins are frozen into one of the deep valleys of free energy. The explanation given in this work is that for site-diluted dipolar systems the nearest neighbours are very often unoccupied and the energy is dominated by weaker forces from distant dipoles [4].

It is clear from previous experimental work that a 20% Ho sample should still be a spin glass (or even a ferromagnet) as 16.7% Ho shows all the behaviour expected of a spin glass. This simulation, however, was carried out on a simple-cubic lattice. It is possible that the tetragonal lattice and other components of the Hamiltonian of $LiHo_xY_{1-x}F_4$ would have the effect of shifting this critical concentration to a point between 4.5% and 16.7%.

4.4 Experimental Examples

One of the 'classical' spin glasses which shows a percolation threshold is the material $Eu_xSr_{1-x}S$. It is a short-range magnet (nearest and next nearest neighbour exchange interactions) which is a spin glass in a range of concentrations from $x = 0.5$ down to $x_c = 0.13$. The point $x_c = 0.13$ is at the percolation threshold of the $Eu_xSr_{1-x}S$ lattice with nearest and next nearest interactions. For concentrations below x_c, the material behaves as a 'super-paramagnet'. The super-paramagnet still shows a strongly frequency-dependent susceptibility (i.e. glassy relaxation) so is not a paramagnet, but it does not have a well-defined spin glass transition temperature. In fact there is even a maximum in the ac susceptibility and it was initially thought that this region was still a spin glass [55]. However, it was found that if a dc measurement is done, the glass freezing transition drops to zero at $x_c = 0.13$ [56]. Much of the physics in $Eu_xSr_{1-x}S$ below x_C is dominated by the dipolar interaction which is much smaller than the exchange interactions [55]. Two distinct rounded cusps are seen in the susceptibility as a function of temperature. It has been

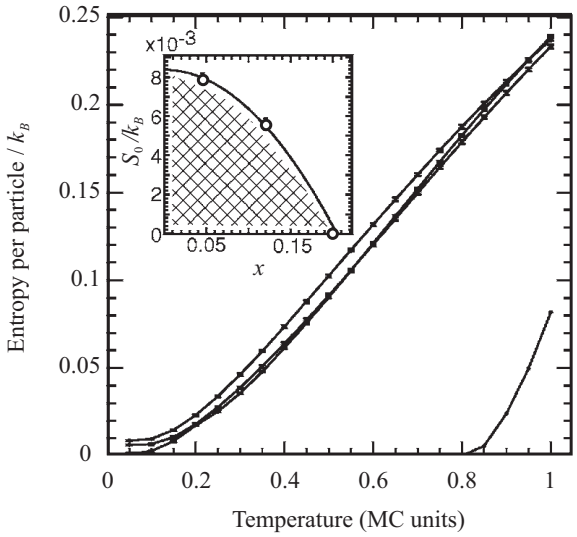

Figure 4.2: Results from the Monte Carlo simulations of Snider and Yu showing the entropy as a function of temperature for several stoichiometries and the residual entropy as a function of concentration in the inset [4].

suggested that there is still a spin glass transition below x_c, but it will be at much lower temperatures because of the weakness of the dipolar coupling [57]. However, the magnetic moment of Eu^{2+} is $5.25\mu_B$ (close to that of Ho^{3+} in the $LiYF_4$ lattice, but isotropic) and yet a spin glass transition temperature is not seen as low as 7 mK [55]. The phase diagram of $Eu_xSr_{1-x}S$ is shown in Figure 4.3.

The RKKY spin glasses like Cu*Mn*, Au*Fe*, Pt*Mn*, Pd*Fe*, etc. are not found to exhibit a percolation threshold. For very small concentrations of the magnetic impurities, a spin glass state is still observed though the transition temperature tends to be very low [59]. This is expected because the interactions in these materials fall off as $1/r^3$ and so are long-range in nature.

The material $LiTb_xY_{1-x}F_4$ is very similar to $LiHo_xY_{1-x}F_4$ in that it is also a diluted dipolar-coupled system. The Tb^{3+} ions, however, are not Ising moments – the ground state doublet is split in energy. This system is also ferromagnetic at $x = 1$ and the T_C is lowered as x is lowered. It has not been shown to become a spin glass at any point, however, and it does have a critical concentration of Tb^{3+} ions $x_C \simeq 0.12$ at which point the T_c drops to zero [60]. A mean-field model of a such a singlet-singlet system is able to describe the phase diagram of the system adequately [61] and it is not expected to behave according to

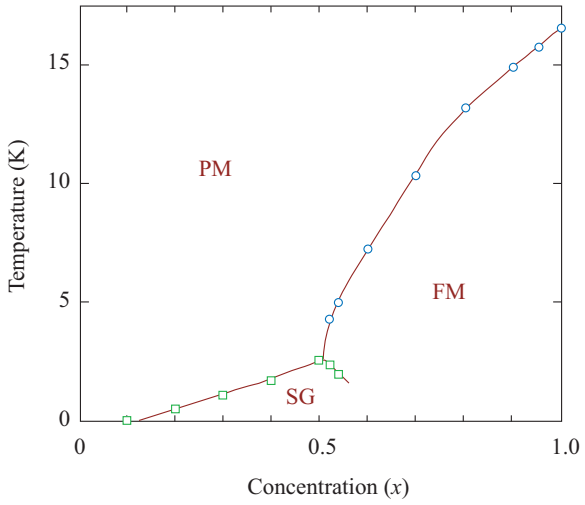

Figure 4.3: The phase diagram of the dilute Ising magnet $Eu_xSr_{1-x}S$. Data points are taken from References [58, 56]. The square symbols are spin glass freezing transitions obtained from a dynamical scaling analysis and the circles are paramagnetic to ferromagnetic transition temperatures found from the position of the cusp in susceptibility.

the theory outlined in Section 4.2.

As was discussed above, dilute dipolar-coupled Ising spins cannot have a percolation threshold and were therefore, for some time, expected to have a finite transition temperature for all x. The material studied here, $LiHo_xY_{1-x}F_4$, however, has been observed to drastically change its magnetic behaviour at $x = 0.045$ despite being dominated by long-range dipolar couplings [1, 2, 3, 62]. This surprising behaviour will be explained in more detail in Section 5.4. Also, as was discussed above, the Monte Carlo simulations of Snider and Yu [4] support the idea that a dipolar-coupled Ising magnet still does have a critical dilution where spin glass ordering ceases to exist at a finite temperature.

Chapter 5

Previous Work on $LiHo_xY_{1-x}F_4$

In the parent compound, $LiHoF_4$, the ferromagnetic interactions dominate and the moments order ferromagnetically at 1.53 K [6]. As one reduces the concentration of the holmium ions (x), T_C is lowered. Materials with $x = 0.67$, $x = 0.44$ [1] and $x = 0.30$ [63] have been studied previously and have paramagnetic to ferromagnetic transitions at 0.98 K, 0.68 K and 0.36 K respectively.

When the moments are sufficiently diluted, frustration due to competing ferromagnetic and antiferromagnetic interactions becomes important. Randomness and frustration are the two main ingredients required for a spin glass (SG) state which has been observed at $x = 0.167$ [1, 9, 10].

At even lower dilution, $x = 0.045$, some very unexpected behaviour has been observed in previous experiments which is the primary motivation for this work and will be discussed in detail in Section 5.4. A current phase diagram of $LiHo_xY_{1-x}F_4$ is shown in Figure 5.1.

5.1 Parent Compound

Pure $LiHoF_4$ is an excellent example of a dipolar-coupled Ising magnet with a transition temperature of 1.53 K. Renormalization group theory finds that the upper critical dimension of a dipolar-coupled system is $d^* = 3$ instead of the usual 4, so that the critical behavior at the transition is expected to have logarithmic corrections $\chi \sim t^{-1}|\ln t|^{1/3}$ to mean-field critical behaviour $\chi \sim t^{-1}$ [53]. For higher dimensions above the upper critical dimension, the usual mean-field exponents are expected to apply. $LiHoF_4$ and the related compound $LiTbF_4$ have been studied in various ways as a test for the predicted corrections, in some cases successfully [5, 64]. Dipolar-coupled Ising magnets are one of the few examples of systems where the upper critical dimension is accessible. With short range

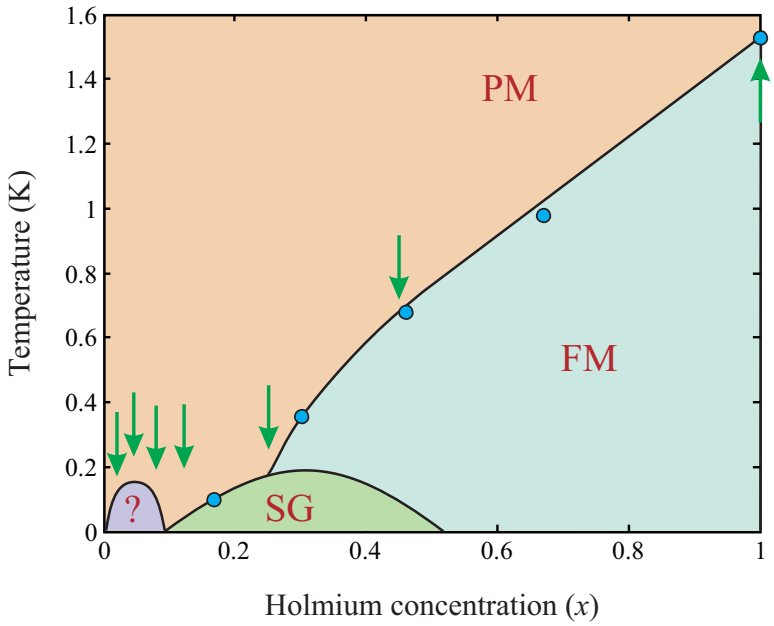

Figure 5.1: The proposed phase diagram of $LiHo_xY_{1-x}F_4$ showing paramagnetic (PM), ferromagnetic (FM), spin glass (SG) "anti-glass" (?) phases. Points are taken from Reich *et al.* [1] (16.7%, 44% and 67%), Bitko *et al.* (100%) and Kjaer *et al.* (30%) [63]. The green arrows indicate samples that we have obtained.

interactions, for example, $d^* = 4$ which is clearly not physical. In measuring the magnetization or susceptibility, however, it is found to be very difficult to discern the logarithmic corrections from the ordinary power-law behaviour [65]. This is an experimental issue and the corrections are much more obvious in Monte Carlo simulations [66].

More recently, this material has been studied as an example of the transverse field Ising model (TFIM) whose effective Hamiltonian is given by

$$\mathcal{H} = \sum_{ij} J_{ij} S_i^z S_j^z - \Gamma \sum_i S_i^x. \tag{5.1}$$

A field applied perpendicular to the c-axis (easy axis) introduces coupling between the ground state Ising doublet and the next nearest excited state and creates a splitting Γ in the ground state energy. This coupling leads to quantum fluctuations which eventually destroy the ferromagnetic order. Even at close to zero temperature, there is a transition or quantum critical point at $H_\perp = 4.9$ T [6].

The critical behaviour of the material in transverse field was studied by Bitko *et al.* [6] by measuring the ac susceptibility of the material using a conventional susceptometer. In zero field, $\chi'(T)$ is found to diverge with the power law $t^{-\gamma}$ where $\gamma = 1$. In other words, it is very close to mean field theory as was seen previously [65]. At constant temperature, $\chi'(H_\perp)$ also shows a sharp cusp at the transition from ferromagnet to paramagnet. At all temperatures studied, the critical behaviour is $\chi \sim h^{-\gamma}$ where $\gamma = 1$ and $h = (H_\perp - H_\perp^C)/H_\perp^C$. There are no signs of logarithmic corrections in the quantum critical behaviour thus the $d = 3$ quantum transition appears to behave as a $d = 4$ classical transition. This is expected theoretically since quantum phase transitions can be mapped onto classical phase transitions in 1 higher dimension [67, 24].

This method also allows one to map out a $(T, H_\perp)$ phase diagram of the material which is shown in Figure 5.2. Bitko *et al.* present a theoretical phase diagram generated by solving the mean-field Hamiltonian

$$\mathcal{H}_{MF} = \mathcal{H}_{CF} + A\mathbf{I} \cdot \mathbf{J} - g_J \mu_B B_\perp J^x - 2J_0 \langle J^z \rangle J^z \tag{5.2}$$

self-consistently. This phase diagram is found to fit the data well if J_0 is used as a fitting parameter. The nuclear hyperfine interaction is found to be fundamental to the low-temperature physics of this system near the quantum critical point.

Chakraborty *et al.* [15] are more rigorous in their treatment of the phase diagram. They develop the effective spin-1/2 Hamiltonian from the crystal field energies and then develop a mean-field theory and quantum Monte-Carlo simulations. Without leaving any fitting parameters, they reproduce qualitative features of the experiment but see less quantitative agreement as the critical field is much higher in experiment than in theory.

5.2 Glassy Ferromagnet

Initially, dilution of the Ho moments simply seems to lower the T_C of the system. At $x = 0.44$, this material is found to be a ferromagnet with a sharp cusp in the ac susceptibility at 0.68 K [1]. In zero field, but at lower temperatures ($\sim$ 0.1 K) there is a peak in χ'' which may indicate some reentrant behaviour where degrees of freedom not locked away in ferromagnetic order freeze as a spin glass [68].

If a transverse field is applied, the system becomes much more complicated. There is a region where glassy dynamics are observed from the frequency response of the ac susceptibility [7, 69]. The system's behaviour shows a dependence on the way in which it is cooled. If it is cooled in a high transverse field where there are strong quantum fluctuations and the field is then turned off, the system is "annealed" quantum mechanically. If the system is cooled in zero field, on the other hand, the system is annealed classically. As a glassy system, it can be thought of as having a very complex free energy surface. Classically it must be thermally excited out of valleys in this free energy surface in order to find its ground state. Quantum mechanically, it can tunnel through barriers resulting in a very different end state. A proposed $(H_\perp, T)$ phase diagram is shown in Figure 5.2 [7, 69].

In a later reference [8], the primary conclusion is that the glassy dynamics stem from domain-wall tunneling. The ferromagnetic domain walls can be thought of as particles sitting in a potential energy surface. The transverse field tunes the mass of this particle and allows it to tunnel between minima in the potential energy surface. In zero field, thermal excitations are required to move the domain walls.

5.3 Spin Glass Phase

An $x = 0.167$ sample from this series was also studied by Wu *et al.* [9, 10]. These works are the first tests of the effect of quantum fluctuations (from transverse field) on a spin glass state. In zero field [1], this sample has been observed to behave essentially just as a spin glass is expected to behave.

The frequency-dependent ac susceptibility was measured in this sample for many frequencies and temperatures [1]. At a given frequency $\chi'(T)$ shows a rounded cusp at the temperature $T_f(\omega)$ which moves to lower temperatures as the measurement frequency is lowered. This cusp obeyed an Arhenius law over the temperature range studied.

The absorption spectrum $\chi''(\omega)$ is a broad curve (several decades wide) which is well fit by a distribution of energy barriers to relaxation. As the temperature is reduced, the spectrum shifts to lower frequency and the distribution of energy barriers becomes wider. A plot of this data is shown in Figure 5.3(a) from Ref. [1]. This is typical of other glasses

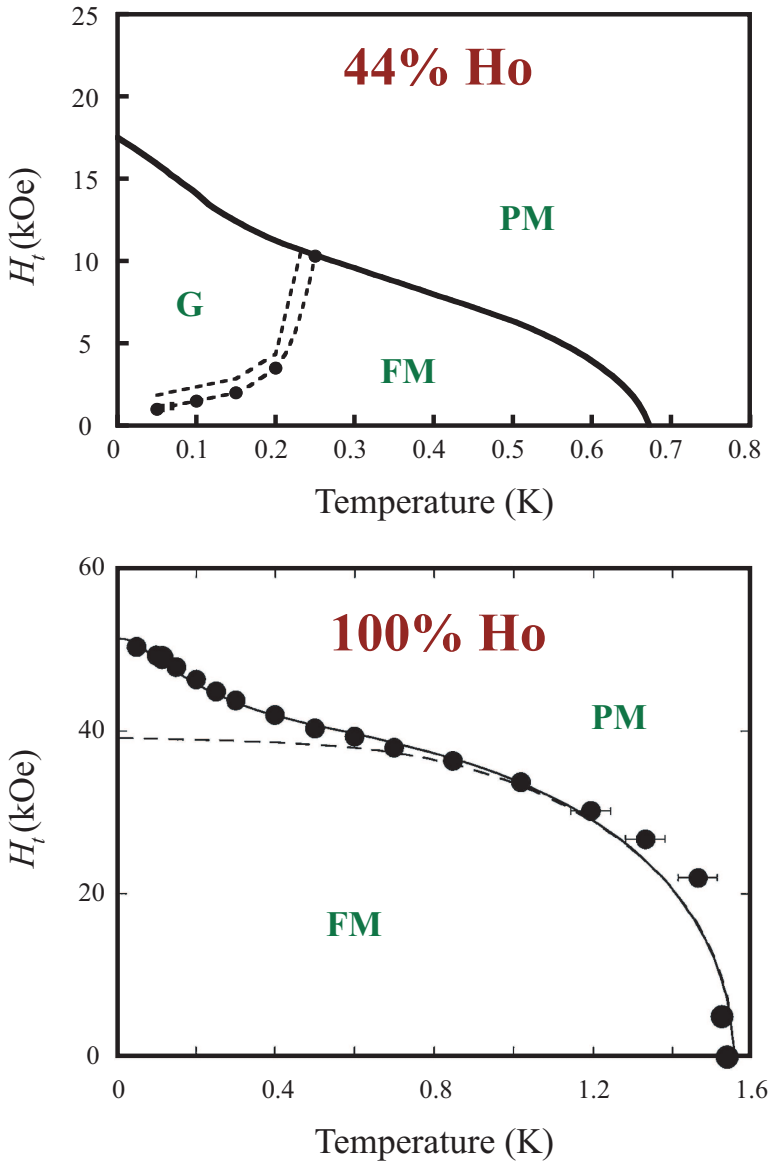

Figure 5.2: Experimental phase diagrams in transverse field (H_t) and temperature (T) of $LiHoF_4$ from Ref. [6] and $LiHo_{0.44}Y_{0.56}F_4$ from Refs. [7, 69].

and the dielectric susceptibility of structural glasses [70, 42].

The specific heat was also measured and after subtraction of the large nuclear component (which will be discussed in Section 6.1), was found to be a broad curve also typical of spin glasses (shown in Figure 8.7).

This material appeared to go through a spin glass transition in transverse field $H_\perp$ as well. The transverse field allows quantum fluctuations to occur (as in the pure material), opening up new routes to relaxation and preventing the spins from freezing. This apparent transition in $H_\perp$ has been measured in two ways: with the frequency dependence of χ'' [9] and with the non-linear susceptibility χ_{nl} [10].

Above the spin glass transition T_g, the effect of a transverse field is simply to narrow the absorption spectrum $\chi''(\omega)$ and to shift $f_{\rm peak}$ to higher frequencies as the quantum fluctuations allow the moments to relax more easily. Below T_g, as $H_\perp$ is lowered, the low frequency behaviour of $\chi''(f) \sim f^\alpha$ is altered with α becoming smaller and eventually reaching 0. Theories have suggested that the spin glass state should be characterized by $\alpha = 0$ [71] and other experiments (on $Eu_xSr_{1-x}S$) have found a very small value < 0.1 for α in the spin glass regime [42]. Thus the point $(H_\perp, T)$ at which $\alpha \simeq 0$ is taken as the spin glass transition (H_c, T_g) [9].

Applying a larger, oscillating longitudinal field h (1.5 Hz and up to 150 Oe in this case), one can observer the field dependence of the susceptibility $\chi_{\rm tot}(h) = \partial M(h)/\partial h$. In a Taylor series expansion $\chi_{\rm tot} = \chi_1 - 3\chi_{nl}h^2 + \ldots$. Thus a quadratic fit to $\chi_{\rm tot}(h)$ will give the quantity χ_{nl} which is directly related to the spin glass susceptibility $\chi_{\rm SG}$.

In this system, $\chi_{nl}(H_\perp, T)$ is found to be a maximum at the transition [10] which is found to be roughly at the same point as was seen using χ'' [9]. As one moves to lower temperatures, the peak in χ_{nl} becomes much smaller and very rounded. Extrapolating these measurements to zero temperature gives a critical field $H_c \simeq 1.2$ T which is equivalent to a ground state energy splitting of $\Gamma_c \simeq 1.0$ K. At zero transverse field, the spin glass temperature is $T_g \simeq 0.13$ K, thus the thermal fluctuations seem to destroy the spin glass order much more easily than quantum fluctuations.

Recent theoretical work on this system has demonstrated the importance of random fields generated by the external transverse magnetic field [72, 73, 74, 75]. It is found that for any finite transverse field, there is no spin glass transition. Instead there are spin glass ordered domains with a correlation length that decreases with increasing transverse field [73]. There does remain a crossover transverse field where the spin-glass order of the domains is destroyed. A mean-field theory incorporating random transverse fields generated by transverse terms in the dipolar and hyperfine interactions was able to reproduce the experimental phase diagram [72]. The smearing of the peak in χ_{nl} at the crossover in larger transverse fields is explained with the random field Ising model and is reproduced numerically [74]. Thus at zero temperature and finite transverse magnetic field, there is

no quantum criticality as a result of the random fields induced in the system.

5.4 Spin Liquid, "Anti-glass" Phase

As was discussed in Section 4.2, for many years it has been thought that random Ising moments coupled by a long-range interaction should not have a percolation threshold [12]. In other words, there should always be some finite temperature at which there is either a symmetry-breaking transition or a spin glass transition for any concentration x. The transition temperature can drop smoothly with decreasing x, but it cannot suddenly drop to 0 at some non-zero x.

The 4.5% sample, measured by Reich *et al.* and Ghosh *et al.* seems to suggest otherwise, as its dynamics are entirely different from the 16.7% sample and what is expected for a spin glass [62, 1, 2]. The primary motivation for the work in this thesis is the goal of eventually understanding the very unusual effects observed in this 4.5% material.

5.4.1 Dynamics

Obtaining equilibrium data on spin glasses can be very challenging in that it requires extremely long times and slow cooling. For the 16.7% sample Reich, *et al.* found that even with a cooling rate of 10 mK per hour equilibrium data was not obtained and the susceptibility was different when warming and cooling. They did find this to be a slow enough cooling rate in order to get equilibrium data for the 4.5% sample however, thus it has somehow a faster response to temperature changes [1].

As with the 16.7% sample discussed above, the susceptibility of the 4.5% sample showed a round cusp in $\chi'(T)$ at T_p which was very sensitive to the measurement frequency f, moving to lower temperatures as f was lowered in keeping with an Arhenius law.

The main difference in the two samples comes from measurements of $\chi''(\omega)$ at a given temperature. At higher temperatures ($\sim$ 300 mK for example) the absorption spectrum is broad like that of the spin glass. But on cooling, instead of widening, the absorption spectrum narrows [62]. The high frequency tail does not change remarkably, but the low frequency behaviour is altered significantly. At first, $\lim_{\omega\to 0}\chi''(\omega) = \omega^{\alpha}$ where α is decreasing with increasing temperature in contrast to the 16.7% sample where it was found to increase with T [1].

Below 120 mK, a power law is no longer adequate because it appears that there is the formation of a gap in the spectrum up to a frequency of 0.1 Hz at 50 mK and up to 1 Hz at 120 mK [2]. This is shown in Figure 5.3(b). At these temperatures, the absorption spectrum is narrower than the absorption spectrum that one would expect for

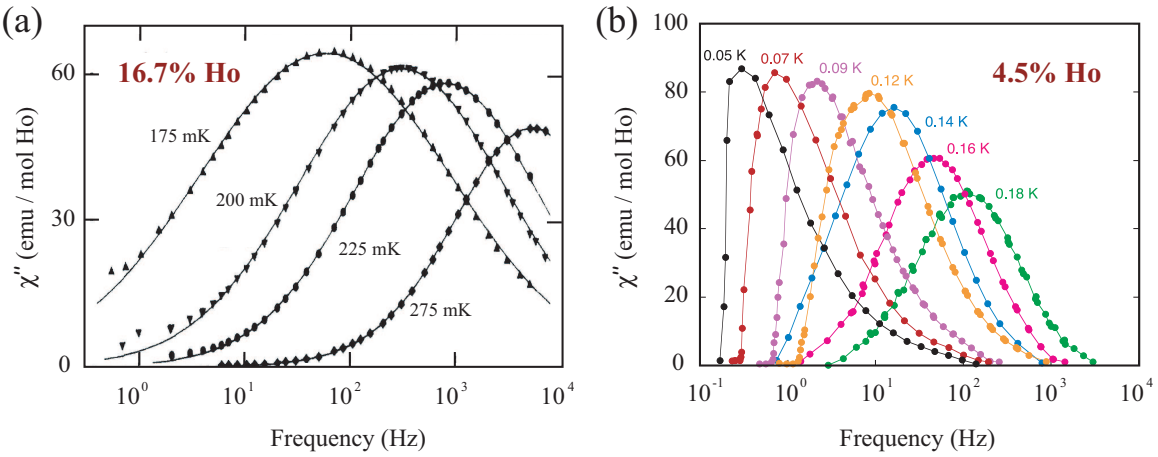

Figure 5.3: The absorption spectra, $\chi''(f)$, of the spin glass (16.7% Ho) from Reich *et al.* [1] and the "anti-glass" (4.5% Ho) from Ghosh *et al.* [2] at several temperatures. The spin glass shows a spectrum that broadens with decreasing temperature where the "anti-glass" exhibits a spectrum that narrows with decreasing temperature. Below 120 mK the 4.5% sample also forms a gap where there is no absorption at low frequency.

a single energy barrier to relaxation. This suggests that, instead, the susceptibility must be originating from a collection of oscillators [2]. The material also begins to deviate from the Arhenius law mentioned above at around 120 mK.

Taking the dc limit $\chi_{\rm dc} = \lim_{\omega\to 0}\chi'(\omega)$, it was found that it looks Curie-Weiss-like ($\chi_{\rm dc} \sim 1/(T-\Theta)$) [1]. Measurements over a larger temperature range, however, show that there is better agreement with the power law $\chi_{\rm dc} \sim T^{-a}$ where $a = 0.75$ [3].

5.4.2 Coherent Oscillations, Hole Burning

Measuring the magnetization as a function of field for an oscillating field of several Gauss gives a Brillouin function $M = Ng\mu_B s\tanh(ng\mu_B sh/k_BT)$ with $n \simeq 260$. This suggests that the system consists of ferromagnetic clusters of several hundred moments with characteristic oscillation frequencies [2]. A longitudinal field of only about 0.5 Oe is sufficient to saturate the response at a given frequency. It seems that there is a relatively small number of moments that behave with that characteristic frequency so very little field is required to saturate the signal at that frequency.

The application of an oscillating transverse field seems also to be able to saturate the moments with a characteristic frequency as they are able to burn holes in the spectrum [2].

An oscillating transverse pump field $h_\perp$ was applied to the sample at a frequency f_0. A much smaller, longitudinal probe field $h_\parallel$ was swept in frequency and the magnetization was measured. The transverse field seems to effect the resulting spectrum in two ways: it shifts the spectrum to a higher frequency (as a dc transverse field did in the 16.7% sample by adding quantum routes to relaxation) and it burns a sharp hole into the spectrum at the frequency f_0.

Finally, if the pump field $h_\perp$ is oscillated at a frequency of 5 Hz for about 600 s and then stopped, oscillations in the sample's magnetization will persist for 4 to 10 seconds afterwards [2]. These effects are all highly unusual for a glassy magnetic system. They seem to point to a system that has coherent excitations, like spin waves or spinons which one expects to find in spin liquid models. Here, these excitations have characteristic frequencies that are several Hz where spin wave excitations are probed by neutron scattering experiments at frequencies of THz.

5.4.3 Specific Heat

Previous measurements of the specific heat of the same $x = 0.045$ sample in zero field also found some very unusual results. After subtracting a nuclear contribution to the specific heat, Ghosh *et al.* found a very small electronic contribution with two sharp peaks at 110 mK and 300 mK [3]. The specific heat is "small" in that very little (only about 15%) of the expected total entropy $R \ln 2$ in the system is released if one does a numerical integral of C/T over the temperature range studied. That would imply that there is an enormous residual entropy in the system.

A numerical simulation (a pairwise decimation procedure) was performed which resulted in a qualitatively similar specific heat. It was also able to reproduce the power law for the dc susceptibility $T^{-\alpha}$ where $\alpha = 0.75$ [3]. The energies of a pair of spins were calculated using an anisotropic g-factor matrix where $g_\perp = g_x = g_y = 0.74$ and $g_z = g_\parallel = 13.8$. Using this model, there are entangled eigenstates resulting from off-diagonal matrix elements of the Hamiltonian. The same numerical simulation performed without the entangled states gave sharp features but at incorrect temperatures.

5.4.4 Other Experiments

Thermal conductivity measurements of a very similar stoichiometry (4.0% Ho) did not reveal any sharp features like those found in the heat capacity at 110 mK and 300 mK [76]. The measured thermal conductivity was found to be largely consistent with single-ion calculations. One might expect thermal conductivity measurements to show those same features as it is a quantity closely related to the specific heat. This would be especially

true if the features are indicative of excitations which are delocalized (like spin waves for example).

Recent μSR experiments on a 4.5% sample do seem to indicate that there are dynamics in the system which persist down to very low temperatures [77]. The frequency range probed by μSR, however, is in the MHz which is much higher than the frequency range in which the "anti-glass" physics have been observed.

Chapter 6

Single-Ion Specific Heat

6.1 Ising model with Nuclear Component

As was discussed in section 2.1, if the crystal field Hamiltonian is diagonalized by itself, the result is a ground state Ising doublet. The simplest specific heat model, then, involves treating the nuclear contribution to the Hamiltonian, $A\mathbf{I}\cdot\mathbf{J}$ as a perturbation.

Because only J^z has matrix elements in the ground state, the transverse components I^x and I^y are irrelevant and we only require the longitudinal nuclear spin I_z. Thus the nuclear hyperfine interaction simply splits the ground state into 8 energy levels corresponding to $m_I = -7/2 \ldots 7/2$. Because of this large number of degrees of freedom, the specific heat from this nuclear contribution is quite large and can be written as

$$\frac{C_{\text{Nuclear}}}{R} = \left(\frac{\sum_m x_m e^{-x_m}}{\sum_m e^{-x_m}}\right)^2 - \frac{\sum_m x_m^2 e^{-x_m}}{\sum_m e^{-x_m}}, \tag{6.1}$$

where

$$x_m = \frac{1}{k_B T}\left(\frac{A g_{\text{eff}}}{2 g_J} m_I + P m_I^2\right) = \frac{1}{k_B T}(A_\parallel m_I + P m_I^2) \tag{6.2}$$

The result is a broad feature centred at around 200 mK shown as the dashed black line in Figure 6.1. This form was used successfully by Mennenga *et al.* [23] to fit heat capacity data on $LiHoF_4$ below the transition temperature. Their best fit gave the values $A_\parallel = 0.420(10)$ K and $P = 0.002(1)$ K.

In the dilute cases, the Curie temperature $xT_c(x = 1)$ has a similar energy scale to the nuclear hyperfine interaction, thus one would expect the heat capacities due to the coupling between moments to overlap the nuclear heat capacity. In fact they are not separable since the nuclear energy levels can lead to mixing with the next excited energy level thereby

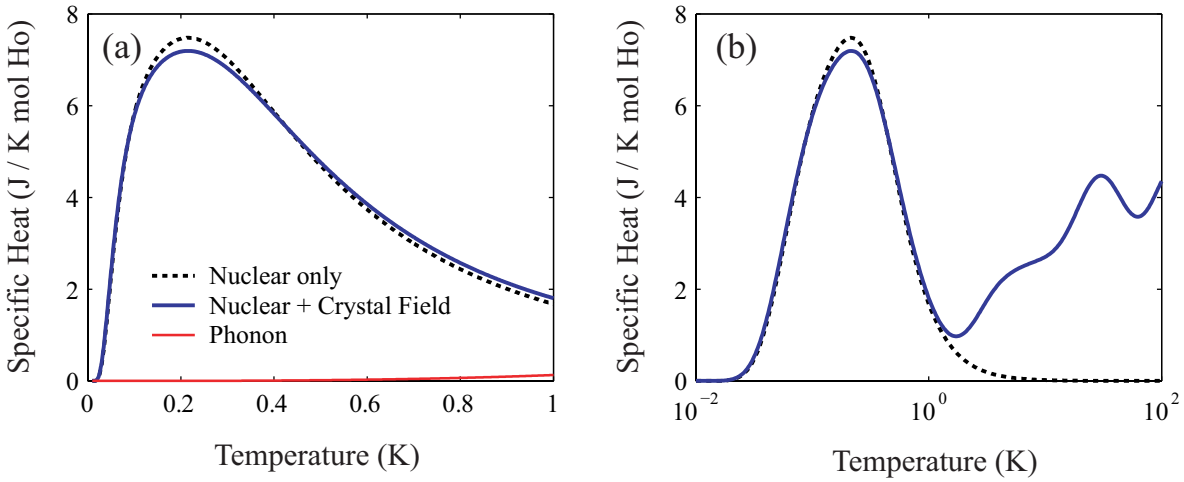

Figure 6.1: Calculations of the non-interacting specific heat over the relevant temperature range (a) and over a larger temperature range (b). The calculation done using only hyperfine energy levels is shown as the dashed black line and the full calculation using crystal field and hyperfine Hamiltonians is shown as the blue, solid curve. The phonon contribution for the 2% sample is shown in red. The phonon contribution for higher concentrations (x) is smaller per mole of holmium.

taking away from the Ising character of the moments [72]. The Hamiltonian is then not diagonal in the J^z basis and the specific heats cannot simply be added together. If it is assumed that the moments are perfect Ising moments, then the specific heat can be written as the sum of a nuclear contribution C_{Nuclear} and an electronic contribution ΔC.

6.2 Full Diagonalization

A more careful calculation of the single-ion (non-interacting) specific heat requires a diagonalization of the non-interacting Hamiltonian

$$\mathcal{H}_{\text{SI}} = \mathcal{H}_{\text{CF}} + \mathcal{H}_{\text{HF}} + \mathcal{H}_{\text{Q}} \tag{6.3}$$

consisting of the crystal field, hyperfine and nuclear quadrupole Hamiltonians. There are 17 electronic angular momentum states ($\mathbf{J}$) and 8 nuclear spin states ($\mathbf{I}$) leading to a 136×136 matrix for the Hamiltonian which is not diagonal in J^z or I^z.

Here we have used $A/k_B = 40.21$ mK which was determined by EPR experiments on $LiHo_{0.02}Y_{0.98}F_4$ [22]. The nuclear quadrupole factor P/k_B has not been determined for

Ho^{3+} in the YLF lattice, but it has been measured to be 1.7 mK with EPR on free Ho^{3+} ions [20]. The crystal field parameters (the B_l^m's) have been taken from Chakraborty *et al.* [15] which were obtained by fitting to spectroscopic data.

The resulting specific heat C_{SI} is quite similar to C_{Nuclear} from equation 6.1, but is smaller by about 4% at some parts in the curve. Both curves are shown in Figure 6.1(a). At higher temperatures the effect of larger crystal field energies is seen as in Figure 6.1(b).

6.3 Effect of Strain on Specific Heat

Holmium ions are non-Kramers ions so are not guaranteed to have a doublet ground state. It is the symmetry of the crystal structure which leads to a degenerate doublet in this case. Altering the symmetry of the crystal field, however, can lead to a splitting of that doublet. Such a energy splitting can be shown to cause a significant change in the single-ion specific heat and could also profoundly effect all of the low-temperature physics in this system.

An effect of certain kinds of strain in the crystal lattice can be to introduce an O_2^2 term (i.e. finite B_2^2) into the crystal field, destroying the S_4 symmetry. Without such a strain there are still pairs of doublets corresponding to different nuclear energy levels, but with such a strain, these doublets are split into distinct energy levels. Since the specific heat at low temperatures is dominated by these nuclear energy levels, the effect can be quite noticeable. Note that a change in the other crystal field parameters such as B_4^0, B_4^{4c}, etc. would not alter the symmetry and would not split the doublets thus the effects would be much smaller.

In order to model the possible effect of strain, we have applied a random degree of asymmetry to the different sites on the lattice. The specific heat for an ion with $B_2^2 = y$ contributes a specific heat $C_i(T, y)$. Then the total specific heat is given by the integral

$$C(T) = \int_{-\infty}^{\infty} C_i(T, y)\rho(y)dy \tag{6.4}$$

where $\rho(y)$ is a Gaussian distribution centred about 0 with a width of σ. The resulting specific heat is shown in Figure 6.2 for several different values of σ. Of course to do this numerically, the integral must be transformed into a summation and for this calculation 100 intervals over a range of $\pm 3\sigma$ were summed. The effect of the lattice distortion is to split the ground state doublet and therefore push some of the specific heat to lower temperatures and some towards higher temperatures. This leads to a drop in specific heat in the centre of the curve at around 200 to 300 mK.

To arbitrarily choose a value in K for the parameter B_2^2 is not sufficient to prove that this is a plausible effect. It is necessary to simulate some sort of quantitative distortion of

the crystal lattice and its effect on the crystal field. In fact a uniform stretching of a given unit cell will not alter the symmetry of the crystal field and so will not contribute a B_2^2 term. A gradient in the crystal strain however, will result in some asymmetry.

We have used a simple model here where adjacent unit cells differ in width by an amount Δ and the stretching is gradual across the cells. The ideal position of the fluoride ions is (x_i^0, y_i^0, z_i^0) and these are translated to give the new positions of the fluoride ions:

$$(x_i^0, y_i^0, z_i^0) \rightarrow (x_i^0[1 + \Delta(x_i^0 + a)], y_i^0, z_i^0). \tag{6.5}$$

This means that a unit cell to the left of a holmium ion has a width (along the x-direction) of a, as usual, but the unit cell to the right of the holmium ion will have a width of $a(1 + 2\Delta a)$.

Once the new fluoride ion positions are calculated, one can calculate the crystal field parameters with the exception of two values: the effective charge q of the fluoride ions (which is simply an overall constant in front of the crystal field Hamiltonian) and the radial integrals $\langle r^n \rangle$ which are nearly impossible to calculate. Fortunately, the same values are used in the crystal field parameters for an unstressed crystal which were adjusted to fit experimental data. So calculating the B_n^m's for an ideal positioning of the fluoride ions, solving for $q\langle r^2 \rangle$ and then putting that into the calculation of the distorted crystal field gives a quantitative value for B_2^2 with a certain amount of distortion in the crystal lattice.

The result of this calculation is that a change in the lattice parameter between adjacent unit cells of about 0.2 Å gives $\Delta = 3.73 \times 10^{-3}$ Å^{-1} and a $B_2^2 \simeq 110$ mK which is sufficient to create a noticeable change in the non-interacting specific heat.

This is a very simple model to get a rough idea of how much distortion is required to create an asymmetry with a relevant energy scale. The details of how crystal strain would occur in the crystal and how it would distort the fluoride ion positions are much more complex and are not known at this time. The quality of the crystals studied here was measured to be very high with X-ray diffraction as will be discussed later in section 7.1. Likely there is not sufficient crystal strain in the samples to create a noticeable change in the specific heat as a 0.2 Å change from one cell to another is very significant and would imply very low crystal quality. Nonetheless, this is an unlikely but possible explanation for discrepancies between our results and previous results which will be discussed in Chapter 8.

6.4 Phonon Specific Heat

The specific heat for the pure material was measured by Mennenga *et al.* up to around 10 K so they were able to look for a T^3 term coming from phonons in the sample [23]. They found $C_{\text{phonon}} = bT^3$ where $b = 5.66 \times 10^{-4}$ J/(K^4 mol Ho). Our measurements are

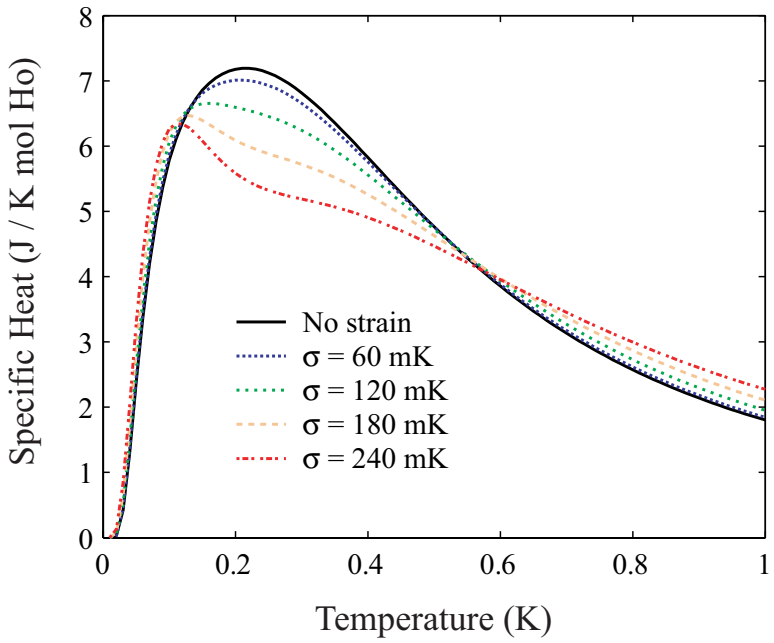

Figure 6.2: The non-interacting (single-ion) specific heat plotted for different amounts of crystal strain (different values of σ).

at much lower temperatures where this would be a very insignificant contribution except for the fact that we are dividing by the number of moles of Ho.

The phonon specific heat should be approximately proportional to the mass of the ions involved. Thus a lattice of entirely Y ions would have roughly half the heat capacity of a lattice of Ho ions (since Y is approximately half the mass of Ho). But if we then divide by the amount of Ho in the system, the specific heat (in units of J/K mol Ho) will be much more significant in a lattice consisting mostly of yttrium. We can estimate the phonon contribution for a material of concentration x to be

$$C_{\text{phonon}} = \left[\frac{x m_{\text{Ho}} + (1-x) m_{\text{Y}}}{x m_{\text{Ho}}}\right] bT^3 \quad \text{(J/K mol Ho)}. \tag{6.6}$$

For low x, the phonon contribution is still small but not completely insignificant in this temperature range. This contribution to the specific heat of the 1.8% sample is shown as the red curve in Figure 6.1.

Chapter 7

Experiment

7.1 Samples

Samples of Ho:YLF were obtained commercially[1], available as high quality single crystals for laser applications. The following stoichiometries have been purchased: 2.0%, 4.5%, 8.0%, 12%, 25%, 45% and 100% Ho concentration. They were grown using the Bridgman crystal growth technique. This technique involves gradually moving an ampoule containing the melt of ingredients through a temperature gradient so that the melt gradually solidifies as a single crystal at one end of the ampoule. A small piece of single crystal is used to seed the growth at the cold end of the ampoule. In the case of this material, the crystal growth must be done in a hydrogen fluoride (HF) atmosphere. Cylindrical crystals on the order of 1 cm in length and 1 cm in diameter were obtained.

Some rare earths are not as miscible with Y in the R:YLF (where R is the rare earth ion) and form stoichiometric gradients from hot to cold in the Bridgman furnace. Ho, however, is very similar to Y in ionic radius and is expected to randomly replace Y in the YLF lattice with very little change to the lattice [1].

During crystal growth, the amount of material lost to evaporation was monitored and no significant amount was observed. The precision of the stoichiometry of the crystals should therefore be quite high. Nonetheless, as will be discussed later in Section 8.2.1, a portion of the 2% sample was found to be closer to 1.8% from measurements of its specific heat. Chemical analysis was performed using both EDS (Energy Dispersive Spectroscopy) with an *EDAX Pegasus* 1200 on a *LEO* 1530 SEM and ICP-MS (Inductively Coupled Plasma Mass Spectrometry)[2]. Both analysis techniques confirmed the stoichiometry of the crystals

[1]Crystals were purchased from TYDEX J.S.Co., St. Petersburg, Russia

[2]ICP-MS measurements were conducted by ActLabs, Ancaster, ON

to be roughly correct, but the systematic errors in the measurement were high and so did not provide as accurate a measure of the stoichiometry as our specific heat measurement. For example, in the EDS measurement, the angle at which the sample surface was oriented was found to change our measurement of the the concentration x by as much as ± 0.005. This was likely due to differential absorption of the electron beam.

Alignment of the crystals was accomplished by two different methods. As large, cylindrical samples, orientation is easily accomplished optically as the materials are optically active and the c-axis is the birefringent axis. Thus if the sample is placed between crossed polarizers, the orientational dependence of the transmission can be used to find the c-axis. Of course refraction and reflection at crystal surfaces influences the transmission as well so this method is not so easily accomplished with smaller, cut pieces of crystal. For that, X-ray Laue patterns were used to orient the crystals. Alignment was only necessary for the susceptibility measurements in this work as the specific heat measurements were performed in zero magnetic field.

The crystal quality has been measured using an X-ray diffraction rocking curve to measure the width of the Bragg peak[3]. The $(2, 2, 0)$ and $(4, 4, 0)$ peaks of the 8.0% sample were measured and were found to be narrower than instrument resolution which was limited to $\simeq 0.03^\circ$. This indicates a very small mosaicity and thus the samples are of very high structural quality. The $(2, 2, 0)$ peak is shown in Figure 7.1. More detailed sample characterization is in progress.

7.2 Low Temperature Apparatus

Two cryostats have been used for the measurements in this thesis. Susceptibility measurements were performed on a Janis ^{3}He Cryostat and heat capacity experiments were done on a S.H.E. Dilution Refrigerator.

7.2.1 ^{3}He Cryostat

The ^{3}He fridge, as its name implies, uses the lighter, rarer isotope of helium to cool. The fridge is inside of a vacuum can which is immersed in liquid ^{4}He. The ^{3}He pot is connected by a stainless steel tube, through a 1K pot, to a charcoal adsorption pump and to an external storage bottle. Initially the charcoal is heated to above 40 K to evaporate the ^{3}He which condenses on the 1K pot and drips into the ^{3}He pot. Once the condensation is complete, the charcoal is cooled and acts as a pump, cooling the fridge to a base temperature of under 250 mK.

[3]Measurements were done by Stefan Kycia and Ariel Gomez at the University of Guelph

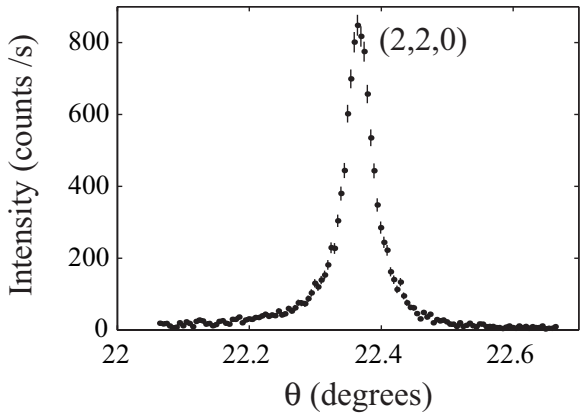

Figure 7.1: The $(2, 2, 0)$ Bragg peak of the 8% Ho:YLF sample studied here. The width of the peak is less than 0.03 degrees (instrument resolution) which indicates very high sample quality.

This is a "one-shot" process – when the ^{3}He as all pumped out of the pot, the fridge no longer has any cooling power so warms up and must be refilled. The cryostat is able to stay cold for roughly 20 hours depending on how much heat is put into the system. Temperature control is accomplished by connecting a stage (which holds a thermometer, heater and experiments) to the ^{3}He pot with copper wire and applying heat with the heater to bring its temperature above the base temperature of the fridge.

7.2.2 ^{3}He/^{4}He Dilution Refrigerator

A dilution refrigerator operates in a very different way. It is also immersed in liquid helium and precooled with a 1K pot, but below that is the dilution unit which operates with a mixture of ^{3}He and ^{4}He. When a mixture of the two isotopes of helium is cooled to below 870 mK, it will separate into two phases: a dilute phase consisting primarily of ^{4}He and a concentrated phase consisting of mostly ^{3}He. As $T \to 0$, the concentrated phase approaches 100% ^{3}He. The dilute phase, on the other hand, approaches a mixture of 6.5% ^{3}He in ^{4}He [78]. The mixing of liquid ^{3}He into liquid ^{4}He is a first-order phase transition with an enthalpy of mixing.

The lighter, concentrated phase naturally floats on top of the dilute phase and during ideal operation, the boundary between the two phases is situated in the middle of the mixing chamber of the fridge. ^{3}He is pumped out of the dilute phase through the "still" and is then returned to the top of the mixing chamber via an impedance. In between the

mixing chamber and still, the incoming and outgoing mixtures are passed through heat exchangers so that the returned ^{3}He is precooled as much as possible. As ^{3}He is pumped out of the dilute phase in the still, ^{3}He enters from the concentrated phase in the mixing chamber such that the concentration stays constant. This results in warming in the still, but cooling in the mixing chamber. To increase the cooling power, the still may be heated to increase the evaporation of ^{3}He and therefore the circulation rate of the fridge.

This particular dilution refrigerator can reach a base temperature of just under 15 mK with an optimal circulation rate of about 50 μmol/sec.

7.3 Conventional Susceptometer

A conventional susceptometer (as opposed to a SQUID susceptometer) depends on magnetic induction to detect the susceptibility of a material. It typically consists of a primary or excitation coil which is used to generate an oscillating magnetic field $Be^{i\omega t}$. Inside the primary is the secondary or pick-up coil. The changing magnetic field will generate a voltage in the secondary coil which is proportional to the derivative of the magnetic flux with respect to time $\partial\Phi/\partial t$. The resulting signal therefore is proportional to the frequency of the oscillating field ω.

Typically, the secondary is wound in a configuration known as a gradiometer. A 1st order gradiometer consists of two counter-wound coils such that a spatially homogeneous field will not generate any net signal. If a magnetic sample is placed inside one of those coils, however, the balance of the gradiometer will be altered by the sample's susceptibility and an oscillating voltage will be measured:

$$\mathcal{E}(t) \propto i\omega\chi(\omega)Be^{i\omega t} = \omega(i\chi' - \chi'')Be^{i\omega t}. \tag{7.1}$$

Thus the component of the signal which is in phase with the excitation is the absorption of the sample $\chi''(\omega)$ whereas the out-of-phase component is the real part of the susceptibility $\chi'(\omega)$.

A 2nd order gradiometer may also be employed to improve noise cancelation and to reduce the offset due to an imperfectly balanced gradiometer. In this configuration, three coils are used with centre coil wound opposite to the two end coils. The number of turns in each of the coils is chosen such that this gradiometer will cancel both a homogenous field and a field gradient. The sample is then placed inside the middle coil. Higher order gradiometers are also possible.

Here we have employed an excitation coil with a diameter of 1.7 cm, a length of 9.5 cm and 830 turns of 75 μm diameter NbTi (superconducting) wire. The secondary was a first-order gradiometer. The two secondary coils were 0.85 cm in diameter and 1.9 cm long with

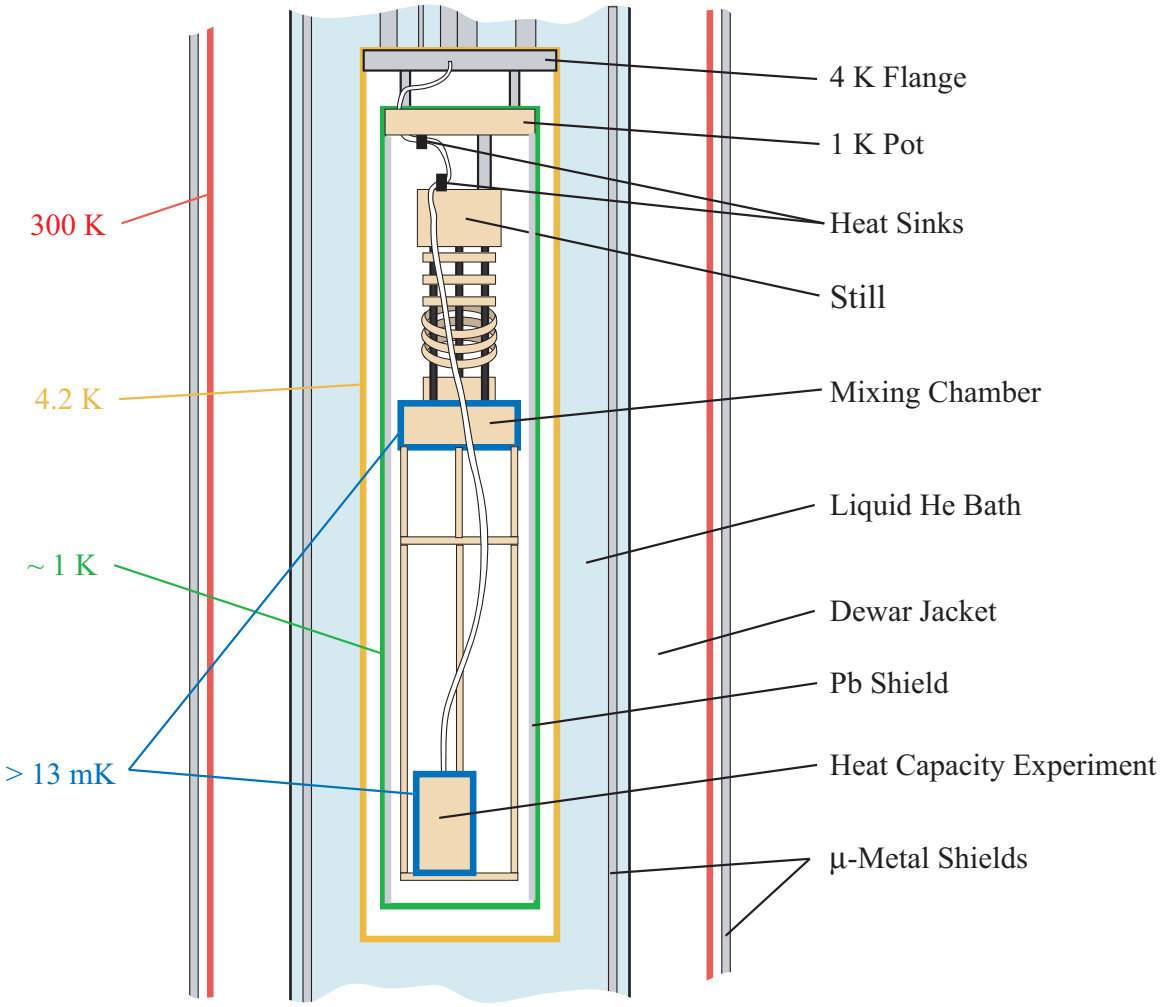

Figure 7.2: Schematic diagram of the cryogenic system used for heat capacity measurements. White space is evacuated for thermal isolation, blue is the bath of liquid helium. The heat capacity cell is contained inside of a copper radiation shield which is thermally connected to the mixing chamber of the fridge and can therefore be cooled to as low as 15 mK.

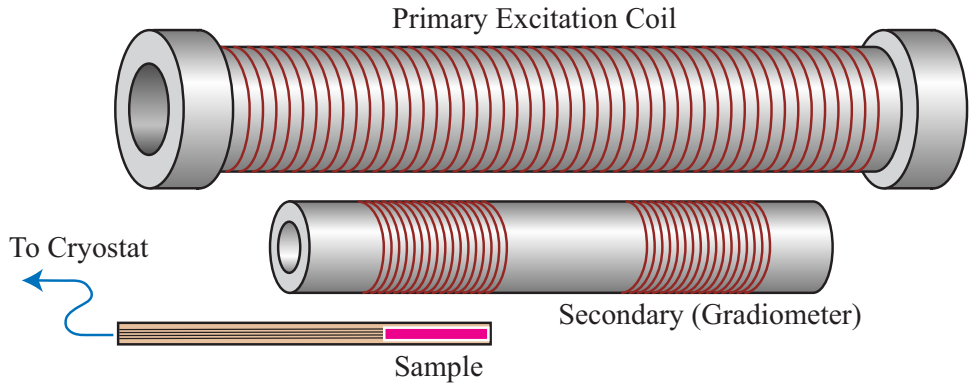

Figure 7.3: A diagram of the conventional susceptometer used for ac susceptibility measurements of 45% Ho:YLF. The excitation coil surrounds the secondary gradiometer which contains the sample. The sample is heat sunk to the cryostat with a bundle of copper wire.

800 turns of copper wire[4]. The coils were separated by 3.8 cm. A sample of $LiHo_{0.45}Y_{0.55}F_4$ was fixed to one end of a bundle of thin insulated copper wires with GE varnish. The other end of the copper wire was heat sunk to the stage of the ^{3}He cryostat. A bundle of isolated wires was used instead of one thick wire in order to reduce the heating from magnetic eddy currents. The sample was needle-shaped with the long direction parallel to the c-axis so as to reduce demagnetization effects. An SR830 Lock-in amplifier was used to apply the oscillating current and measure the resulting signal as the temperature of the sample was changed. A frequency of 1 kHz was used for these measurements.

7.4 Heat Capacity Measurements

There are three main approaches to the measurement of heat capacity:

1. *The quasi-adiabatic method.* In this measurement, a heat pulse Q is applied and the rise in temperature ΔT of the sample is measured. It would be difficult to create a completely adiabatic heat pulse as the sample must in some way be connected to the dilution fridge in order to get cold in the first place. Thus in this experiment one must account for the heat lost during the heat pulse.

2. *The relaxation method.* The relaxation method involves observation of the time constant of relaxation of the sample's temperature towards the temperature of a

[4]The susceptometer used for these measurements was constructed largley by Lauren Lettress

thermal bath (the cryostat). If the sample has a heat capacity C and the thermal conductance of the link between sample and cryostat $K = \kappa A/L$ is well known then measuring the time constant of relaxation $\tau = C/K$ will give one the heat capacity of the sample.

3. *The ac method.* This method involves the application of a variable, oscillating heat $\dot{Q}(t)$ and the observation of temperature as a function of time $T(t)$. This is analogous to the application of an ac current to a RC-circuit and measurement of the voltage. The out-of-phase component of the oscillating temperature will be related to the heat capacity of the sample.

Measurements for this work were done using the quasi-adiabatic method. This method was chosen so that time constants within the sample (due to poor thermal conductivity, spin-lattice relaxation, etc.) would not interfere with the heat capacity measurement. In real structural glasses the heat capacity can have a slow relaxation [79] and indeed in these samples we have observed some unusual non-equilibrium effects with time constants of several minutes which will be discussed later in further detail. Poor thermal conductivity within the sample can also lead to a slow response. These time constants can be measured and separated out if one is using a long enough time constant of relaxation as is preferable in the quasi-adiabatic method. In the other heat capacity experimental methods one needs to wait at least one time constant for every data point, so use of a very long time constant would be extremely time consuming.

7.4.1 Physical Apparatus

In designing the experimental apparatus for these measurements, very close attention was paid to the thermal conductivity and heat capacity of various components of the apparatus to eliminate potential heat leaks and other sources of error. Unlike in most heat capacity experiments, no substrate was used – all components were fixed directly to the sample itself which was floating on very thin nylon threads. If the thermal conductivity between a sample and the substrate is poor then there can be errors in the temperature measurement. Additionally, a substrate can add a significant addendum which then needs to be measured and subtracted from the data.

The thermometers were RuO_2 resistors (1 kΩ resistance at room temperature) with thinned alumina substrates. Heaters were 10 kΩ metal-film resistors (also with their substrates polished away as much as possible to improve thermal contact and reduce heat capacity). Resistors were glued to the sample with GE varnish. Leads to the thermometers and heaters were 6 μm NbTi, superconducting wires, each about 0.5 cm in length.

These were made by dissolving the copper-nickel cladding of multifilamentary NbTi magnet wires in nitric acid. The leads were attached on either end with silver epoxy. These leads were chosen to keep their thermal conductivity extremely low. The thermal conductivity of the electrons in a superconductor drops out exponentially below T_C ($\sim$ 10 K for NbTi) as the superconducting electrons do not conduct heat. The fact that the wires are made from a disordered alloy means that the RRR of the metal is poor (often $\sim$ 1 for NbTi) so the remaining normal electrons also conduct less heat than in a clean metal (like pure Nb for example). Additionally, they have an extremely small diameter which greatly increases their thermal resistance.

The weak thermal link from the sample to the mixing chamber of the dilution fridge was made from a short length of Manganin wire which was also fixed on either end with silver epoxy. This weak link was chosen to have a thermal conductance K_{WL} such that the time constant of relaxation $\tau = C/K_{\mathrm{WL}}$ would be longer than an hour over most of the temperature range studied. Since $\kappa \sim T$ and C varies significantly, the time constant is fairly different in different temperature ranges. At low temperature the heat capacity is dropping out quite quickly, but Kapitza thermal boundary resistances between conductor and insulator ($\kappa \sim T^3$) become important so the time constant remains quite long.

Thermal conductances and heat capacities for various components are given in Table 7.1. These parameters were calculated or measured in various ways. For example, the heat capacity of the heater and thermometer were estimated based on the size of the alumina substrate and metal pads. The thermal link between thermometer and sample, on the other hand, was determined by applying a large enough excitation to the thermometer to cause heating and measuring the time constant of relaxation of the thermometer's temperature with respect to the sample temperature. The heater was assumed to be very similar to the thermometer in terms of heat capacity and thermal conductivity.

7.4.2 Experimental Procedure

Heat capacity data is obtained by applying heat pulses of a known size via the heater and observing the change in temperature of the sample. A voltage is applied across a large current limiting resistor (typically $\sim$ 1 MΩ) in line with the heater with an analog output channel of a National Instruments DAQ-card. This heat "pulse" is usually 1 to 2 minutes in length. This length is chosen so that a reasonably small power is applied and the superconducting leads are not driven normal. Measuring the voltage across the heater during the heat pulse shows that the leads do in fact remain superconducting. The thermal conductivity may still vary significantly at different temperatures even while superconducting, but in the temperature range studied, should remain very low. The thermometer resistance is measured with a *Linear Research* LR700 ac resistance bridge.

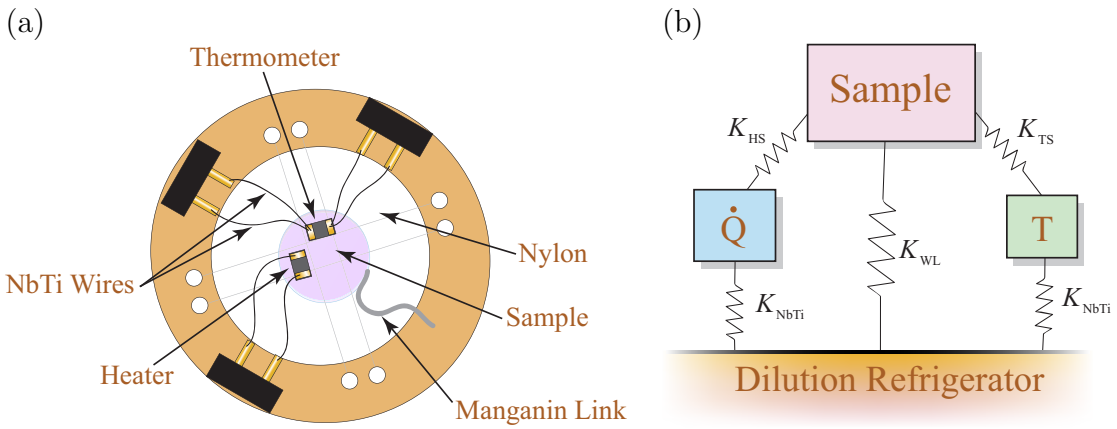

Figure 7.4: (a) Diagram of physical apparatus used for the measurement of specific heat. (b) A simple picture of the heat capacities and thermal links in the system.

To get an accurate measure of the temperature, fits are done to the data before and after the pulse. Since the time constants employed here are very long, linear fits are usually sufficient. At higher temperatures, where the time constant is becoming shorter, quadratic or exponential fits are employed.

During a heat pulse, some of the energy will be lost through the weak link and this must be accounted for when calculating the heat capacity. Suppose that the fit before the heat pulse gives $T(t) = a_0 + b_0 t$ and the fit after the heat pulse gives $T(t) = a_1 + b_1 t$. This means that, by Newton's law of cooling, the rate of loss of heat through the weak link is $b_0 C$ before the pulse and $b_1 C$ after the pulse. To first order, the rate of heat loss during the pulse will be the average of these. Thus the total heat lost during the pulse will be $Q_{\text{lost}} = C\Delta t(b_0 + b_1)/2$. The temperature change from the start of the pulse to the end of the pulse will therefore be

$$\Delta T = Q_{\text{heater}}/C - \Delta t(b_0 + b_1)/2. \tag{7.2}$$

Solving for C, we get that $C = Q_{\text{heater}}/\Delta T_{\text{eff}}$ where T_{eff} is obtained by extrapolating the fits to the midpoint of the heat pulse. An example of a heat pulse and the corresponding linear fits is shown in Figure 7.5. This will be very close to correct provided the time constant is long and linear fits are reasonable. At higher temperatures this is not as good an approximation so it is desirable to reduce the length of the heat pulse.

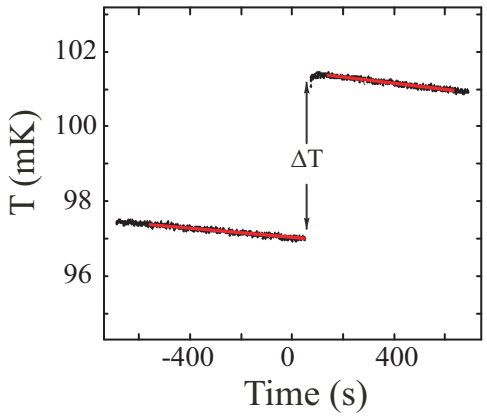

Figure 7.5: An example of temperature data vs. time before and after a heat pulse. The solid red lines are fits to the data done in order to evaluate the temperature change induced by the pulse.

7.4.3 Thermometry

The largest obstacle to good heat capacity data at low temperature is good thermometry. There are several types of thermometers available, none of which is able to easily cover the range of temperatures studied here. Our temperature calibration must therefore come from a patchwork of various thermometry techniques.

A CMN thermometer uses the susceptibility of the paramagnetic salt $Ce_2Mg_3(NO_3)_12 \cdot 24H_2O$ which obeys a Curie-Weiss law $\chi \sim 1/(T - \Theta)$ and may be used from ~ 200 mK down to ~ 5 mK. Since CMN is a paramagnetic insulator, it does not dissipate any heat giving it an advantage over resistive thermometers. We have used a SQUID magnetometer to measure the susceptibility of CMN thermally linked to the fridge with silver foil in order to calibrate more convenient resistive thermometers[5].

Another thermometer employed in this work is the nuclear orientation (NO) thermometer. This thermometer consists of a single crystal of radioactive ^{60}Co. At low temperatures, the electronic moments of Co are ferromagnetically ordered along the c-axis of the crystal. It is energetically favourable for the nuclear moments to align themselves with the electronic moments, but the interaction is weak enough that it has no noticeable effect until around 50 mK. One of the decay paths of ^{60}Co involves the emission of a gamma ray which is emitted preferentially perpendicular to the spin of the nuclear moment. Thus at high temperature, the emission of gamma rays is largely isotropic, but below 50 mK, fewer

[5]CMN sample was grown and prepared by Krizsanta Greco

gamma rays are emitted along the c-axis of the crystal. Nuclear orientation thermometry involves the detection of these emitted gamma rays at room temperature once they have penetrated the dewar. This means that no leads (potential heat leaks) are required for this type of thermometry. The main disadvantage of this thermometer is the long time required to obtain sufficient counts at a given temperature.

From about 75 mK up to several K, a germanium resistance thermometer (GRT) purchased from *LakeShore Cyrogenics* is trusted to give a good measure of the temperature. These thermometers consist of a carefully stress-relieved Ge crystal suspended inside a canister of ^{3}He exchange gas and are very stable with respect to thermal cycling. A disadvantage of GRT's is their complicated temperature dependence which is often fit with splines. For temperatures below 75 mK, the GRT's temperature behaviour was calibrated to the CMN thermometer and nuclear orientation thermometer on one cooldown of the cryostat.

The thermometers used for measuring the sample temperature were 1 kΩ RuO_2 chip resistors chosen for their small size and sharp temperature dependence. The resistance is often given [78], approximately, by the formula

$$\ln R = a + bT^{-\alpha}. \tag{7.3}$$

In practice, the exponent α varies from one batch of resistors to another, and the exact resistance is a more complex function of temperature. Often the formula

$$\ln T = \sum_{n=0}^{3} \alpha_n (\ln R)^n \tag{7.4}$$

is used to fit a temperature calibration and that equation has been used for these measurements.

7.4.4 Modeling the Experiment

A heat capacity experiment can be modeled reasonably accurately using Newton's law of cooling to generate a set of differential equations. This is equivalent to a circuit diagram, shown in Figure 7.6, where thermal resistances are replaced by resistors, heat capacities are replaced by capacitors and heaters are replaced by current supplies. Voltage in the circuit analogy is equivalent to temperature in the actual experiment and current corresponds to heat flow.

In our apparatus one obtains a system of three differential equations:

$$\gamma \frac{\partial T_H}{\partial t} = \dot{Q} - (K_L + K_A)T_H + K_A T \tag{7.5}$$

Component	Thermal Conductance	Heat Capacity
Sample	> 0.01 W/K	4.9×10^{-4} J/K
Weak link (Manganin)	1.36×10^{-7} W/K	$< 7 \times 10^{-8}$ J/K
Thermometer (alumina substrate)	$> 5 \times 10^{-8}$ W/K	1.6×10^{-7} J/K
Heater (alumina substrate)	$> 5 \times 10^{-8}$ W/K	1.6×10^{-7} J/K
Electrical leads (NbTi)	$< 3 \times 10^{-11}$ W/K	Negligible
Nylon threads	8×10^{-9} W/K	Negligible

Table 7.1: Table of typical thermal conductivities and heat capacities for various components of a heat capacity experiment at 100 mK. The values for the sample and weak link here are specific to the 4.5% sample, but similar values apply to the 1.8% and 8% samples as well. The values given here are the worst-case scenario, so actual experimental errors should be equal to or smaller than the errors calculated in this section. The thermal conductivity of $LiHo_{0.04}Y_{0.96}F_4$ was measured by Nikkel *et al.* [76]. Other calculations were made using data from Ref. [78].

$$C\frac{\partial T}{\partial t} = K_A T_H - (K_W + 2K_A)T + K_A T_T \tag{7.6}$$

$$\gamma\frac{\partial T_T}{\partial t} = -(K_A + K_L)T_T + K_A T \tag{7.7}$$

where γ is the heat capacity of the heater and thermometer. The temperatures T_H, T_T and T are the temperatures of the heater, thermometer and sample respectively. This equation can be written more succinctly as a vector equation:

$$\frac{\partial \mathbf{T}}{\partial t} = \mathcal{A}\mathbf{T} + \mathbf{B} \tag{7.8}$$

Making a unitary transformation, we obtain

$$\frac{\partial \mathbf{T}'}{\partial t} = \frac{\partial}{\partial t}U^{-1}\mathbf{T} = (U^{-1}\mathcal{A}U)(U^{-1}\mathbf{T}) + U^{-1}\mathbf{B} = \mathcal{A}'\mathbf{T}' + \mathbf{B}' \tag{7.9}$$

where $\mathcal{A}'$ is the diagonal matrix of $\mathcal{A}$. The solution to the system of differential equations is then

$$T_i' = \left(T_{i0}' + \frac{B_i'}{\mathcal{A}_{ii}'}\right)\exp\left(-\mathcal{A}_{ii}'t\right) - \frac{B_i'}{\mathcal{A}_{ii}'} \tag{7.10}$$

Using the thermal conductivities and heat capacities listed in Table 7.1 and Equation (7.10), a heat pulse can be simulated. The results of such a simulation are shown in

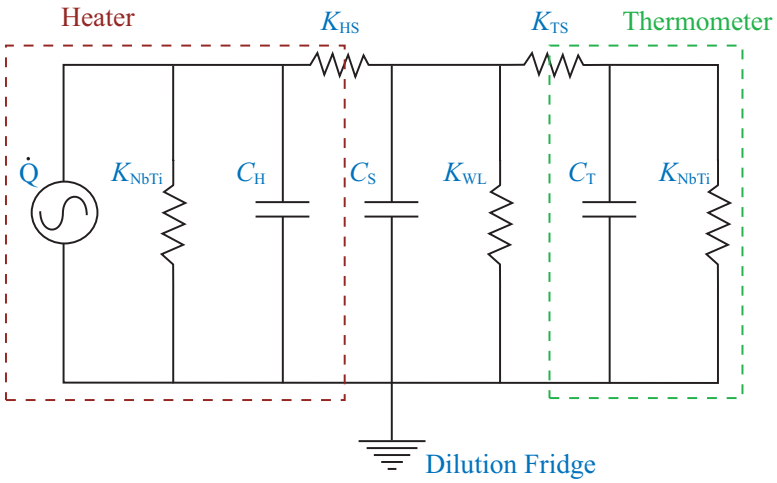

Figure 7.6: The equivalent circuit diagram to our heat capacity apparatus. Resistors correspond to thermal resistances (conductances), capacitors correspond to heat capacities and the current supply is equivalent to the power applied through the heater.

Figure 7.7. We have deliberately simulated a heat pulse at very low temperatures where problems of thermometer decoupling, etc. are most likely. The simulation shows that our measurement of the temperature is roughly 0.03% off from the sample's temperature even at the lowest, most challenging temperatures. The extrapolation to the midpoint of the pulse then results in a 0.2% error in the measurement of ΔT.

7.4.5 Simulation with a Substrate

In a more conventional measurement where the sample, weak link, thermometer and heater are attached to a substrate, the following equations are appropriate:

$$\gamma \frac{dT_H}{dt} = \dot{Q} - (K_L + K_A)T_H + K_A T_S \tag{7.11}$$

$$C_S \frac{dT_S}{dt} = K_A T_H - (K_{SS} + K_{WL} + 2K_A)T_S + K_{SS} T + K_A T_T \tag{7.12}$$

$$\gamma \frac{dT_T}{dt} = K_A T_S - (K_A + K_L)T_T \tag{7.13}$$

$$C \frac{dT}{dt} = K_{SS} T_S - K_{SS} T \tag{7.14}$$

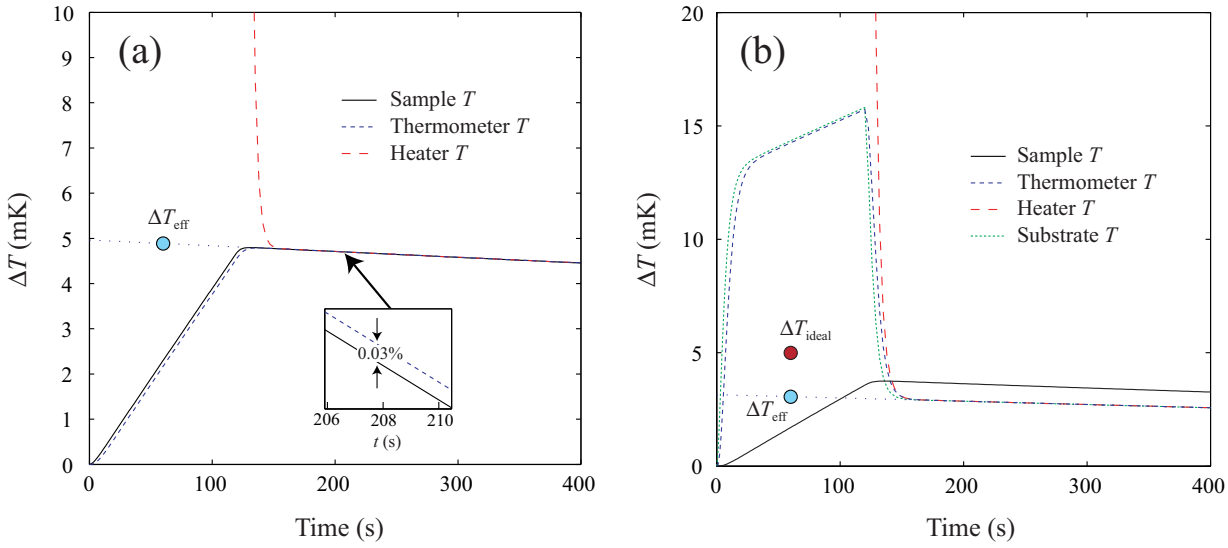

Figure 7.7: (a) A simulation of a heat pulse in our apparatus using equation (7.10). The difference from the fridge temperature ΔT is shown on the y-axis as a function of time. The heat pulse was 120 s long and the magnitude was chosen to give a 5 mK temperature step. Parameters were selected to give a worst-case scenario. Even then, the measurement of the temperature is within 0.03% of the correct sample temperature and the extrapolation to the mid-point of the heat pulse results in only 0.2% error. The error in the extrapolation is largely due to heat lost during the pulse through the heater leads as the heater gets quite hot ($\sim$ 180 mK). In practice, the rise in temperature of the heater will make the thermal conductivity of the alumina much better while the NbTi leads will still be poor thermal conductors as they are well below their transition temperature, thus we expect this error to be even smaller still. (b) A simulation of a heat pulse using a configuration with a substrate. A significant overestimate of the sample's heat capacity results.

where T, C refer to the sample, T_S, C_S refer to the substrate and K_{SS} refers to the connection from sample to substrate. The thermal conductances K_{TS}, K_{HS} and K_{WL} are all taken as connected to the substrate, though it is not expected that these values would be much different from when they were connected to the sample.

Without details of the components used in a certain heat capacity measurement it is impossible to choose exact values for C_S and K_{SS}. We can, however, make some crude estimates. The addendum due to the substrate will generally be under 1% of the sample's heat capacity thus we will choose $C_S = 0.01C$. Samples in our experiments are often platelets with an area roughly 10 times the area of the thermometer chips. Assuming that the conductance from the thermometer to the sample is dominated by a Kapitza boundary resistance, it would be safe to say that $K_{SS} \simeq 10K_A$. Then we can run a similar simulation to that employed in Section 7.4.4, though in this case it will be a set of 4 differential equations.

The result is a serious deviation of the substrate temperature from the sample temperature. During the heat pulse, the substrate is hotter than the sample as heat tends to flow slowly into the sample and is able to flow quickly out of the substrate into the dilution fridge. Once the heat pulse ends, the heat is flowing from sample to substrate and then through the weak link, so the substrate temperature quickly moves to sit between the sample and the fridge temperatures. The result is a significant underestimation of the sample temperature well after the heat pulse. This of course leads to an overestimation of the specific heat of the sample.

In a slightly different configuration where the weak link is connected to the sample instead of the substrate, the opposite occurs: the substrate temperature is above the sample temperature after the heat pulse. In this case, however, the temperature difference is very small since the substrate has a small heat capacity and quickly approaches something close to the sample temperature.

7.4.6 Error Analysis

The dominant source of error in specific heat measurements is in the measurement of temperature. The change in temperature ΔT is often of the order of 5 mK. Thus even a 1 mK error in ΔT could result in a very large error in the heat capacity. The error in the heat capacity measurement mostly comes from the derivative of the error of the temperature calibration. If the temperature before the pulse T_0 and the temperature after the pulse T_1 are incorrect by the same amount, there will be no error in the specific heat axis. The error arises from T_0 and T_1 being off by different amounts or even off by different directions. In other words, the error on the absolute temperature T may be large, but the error on ΔT will be much smaller keeping the error on C in check.

This means that the temperature calibration of the thermometer must be done very carefully. Using a high-order fit, will give good agreement between calibration data and the fit, but will have a steeper derivative in some places to account for scatter in the calibration points. This will significantly distort the specific heat. Thus a reasonably smooth fit must be employed as in Equation (7.4).

We have estimated the maximum likely systematic error in the heat capacity measurement from the residuals after the fit to calibration data. The error in the measured temperature step $\sigma_{\Delta T}$ is given roughly by the derivative of the error in the temperature measurement times the width of the temperatures step, so

$$\sigma_{\Delta T} = \frac{\partial \sigma_T}{\partial T} \Delta T \equiv b \Delta T \tag{7.15}$$

where $d\sigma_T/dT$ is estimated from the maximum slope of the residuals. Then the error in the heat capacity measurement will be

$$\sigma_C = \frac{\partial C}{\partial (\Delta T)} \sigma_{\Delta T} = \frac{\dot{Q}}{(\Delta T)^2} b \Delta T = bC. \tag{7.16}$$

The resulting error is less than 1.2% above 130 mK, about 2.5% at 100 mK and as much as 10% below 80 mK. Estimated error bars are shown in Figure 8.8.

There are several reasons for such a large error at the lowest temperatures. Self heating can cause thermometers to read inconsistently as the noise environment of the system changes. The temperature calibration around 50 mK must be obtained from the overlap of several thermometry techniques: a commercially calibrated GRT, a CMN susceptibility thermometer and a ^{60}Co nuclear orientation thermometer. Joining the calibrations from different thermometers and different temperature ranges is quite challenging. The error in the calibration fit is also intrinsically larger as one moves closer to the edges of the data being fit. Finally, the sample is cooling very slowly at this point, so it can be difficult to determine the point at which the temperature has reached equilibrium with the cryostat's temperature.

If there is significant self-heating in the resistance thermometers, as there often is at very low temperatures, the temperature measurement can significantly effected. It is common for resistors to self-heat by about 5 mK at a temperature of 50 mK. Thus if the sample were at 50 mK, the thermometer would read 55 mK. This error is expected to drop off as T^{-3} since the thermal conductivity of insulators is proportional to T^3. Note that if the self-heating is consistent from one cool-down to the next, the thermometer calibration will take care of it. The noise environment is likely, however, to change from day to day.

A gradual temperature shift does not strongly effect the total specific heat data. However, when we wish to subtract a calculated, non-interacting component to the specific

heat, the result will be very strongly effected by errors in the temperature measurement. Such an effect is also shown in Figure 8.8.

In addition to the systematic error discussed above, there is also a Gaussian scatter to the data. This is attributed largely to the fitting of data before and after the heat pulse which has scatter due to the noise of the resistance measurement. The error on the extrapolation to the midpoint of the pulse is given by the following equation:

$$\sigma^2_{\hat{T}(t^*)} = \left[\sum_i \frac{(T_i - \hat{T}(t_i))^2}{n-2}\right]\left[\frac{1}{n} + \frac{n(t^* - \bar{t})^2}{n\sum_i t_i^2 - \left(\sum_i t_i\right)^2}\right]. \tag{7.17}$$

Here the n points we are sampling are (t_i, T_i), $\hat{T}(t)$ is the estimated temperature at a given point time t (from the linear fit), t^* is the midpoint of the heat pulse to which we are extrapolating and $\bar{t}$ is the average time (and also the midpoint of the fit in this case) [80]. The Gaussian error, calculated in this way, is enough to account for the scatter seen in the plots of $C(T)$. This scatter could be reduced by lowering the noise in the resistance measurement, integrating longer and possibly by improving the stability of the cryostat temperature control.

Measurement of the mass of the sample was done with a very high precision balance, thus this error is insignificant relative to the other errors in the system.

Chapter 8

Results and Discussion

8.1 AC Susceptibility of 45% sample

The ac susceptibility of $LiHo_{0.45}Y_{0.55}F_4$ at 1 kHz as a function of temperature is shown in Figure 8.1. There is a cusp found in $\chi'(T)$ at a temperature of 0.68 K. This cusp is sharp in the temperature resolution studied here and its position was not found to shift in temperature when the measurement frequency was changed to 50 Hz. Thus it most likely signals a transition from paramagnet to ferromagnet. If it were a spin glass, the peak position would depend on the measuring frequency and the cusp would be rounded. No attempt was made to carefully study the frequency-dependence of the susceptibility or extract critical exponents from the data. Above the transition, the real part of the susceptibility can be fit by a Curie-Weiss law:

$$\chi'(T) = \frac{C}{T - \Theta} \tag{8.1}$$

with $\Theta = 0.47$ K. However, demagnetizing effects and an offset in the signal make a good fit to the data difficult and this may explain why the parameter Θ does not match with T_c. Additionally, the range over which the fit is done is only a third of a decade in temperature which is generally not adequate for a good fit of this sort. If this were an antiferromagnetic transition, one would expect a negative Θ.

Nonetheless, the transition temperature of 0.68 ± 0.01 K agrees well with previous measurements of a 44% Ho sample which also exhibited a transition at 0.68 K. This measurement is thus consistent with the proposed phase diagram shown in Figure 5.1. We have not performed measurements on this material to a low enough temperature or high enough magnetic fields to observe the glassy effects that were previously seen [7, 8].

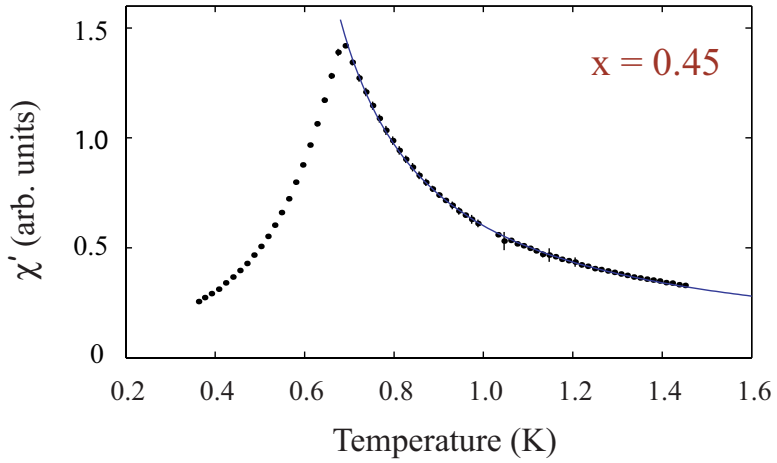

Figure 8.1: The complex ac susceptibility of $LiHo_{0.45}Y_{0.55}F_4$ as a function of temperature, measured at 1 kHz. The solid, blue line is a fit of the form $\chi'(T) = C/(T - \Theta)$ with $\Theta = 470$ mK.

8.2 Specific Heat at Low Concentration

The measured heat capacity of $LiHo_xY_{1-x}F_4$ is dominated by the broad nuclear hyperfine contribution which was calculated in Section 6.2. There is an additional contribution from the electronic interactions on top of this. The total specific heat is shown in Figure 8.2 for $x = 0.018$, $x = 0.045$ and $x = 0.080$ from ~ 75 mK up to 0.8 K. The curves are very close for much of the temperature range studied. The difference comes largely at the peak of the curve where the specific heat is smaller with lower x.

8.2.1 Subtraction of the Nuclear Contribution

In order to more closely observe the effect of the dipolar interactions on the specific heat, we have subtracted away the single-ion (non-interacting) specific heat $C_{\rm SI}$ which was calculated in Section 6.2 leaving a smaller component ΔC. If the system is assumed to be a perfect Ising model, this subtraction is completely justified as transverse components of the hyperfine and dipolar interactions are not important. In practice, however, the transverse parts of the Hamiltonian are important and the interacting and non-interacting specific heat are directly connected and cannot be separated. We will, nevertheless, present the subtracted data in the hope that it is still largely indicative of the behaviour of the electronic moments in the system and to check for consistency with previous publications

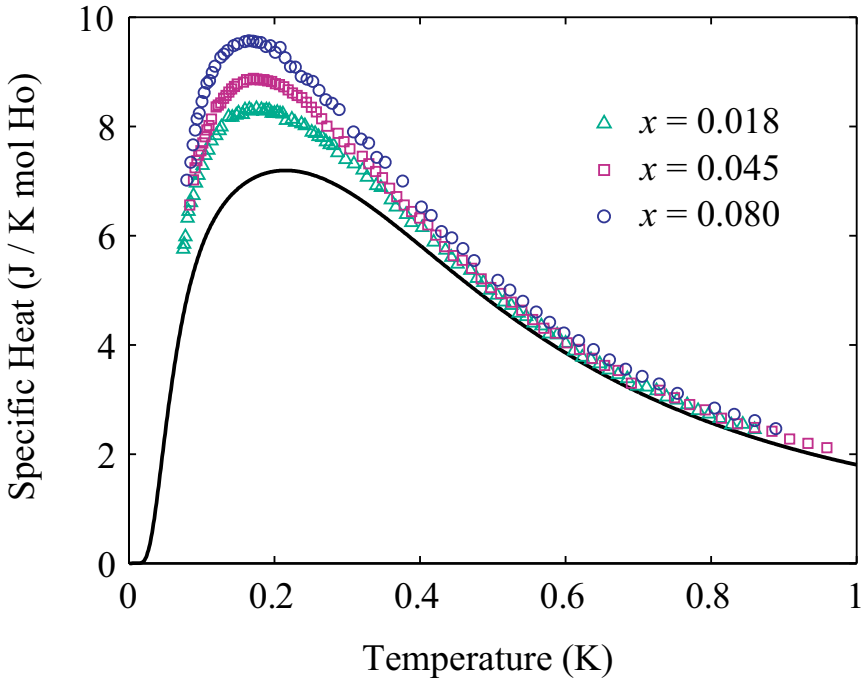

Figure 8.2: The total specific heat of $LiHo_xY_{1-x}F_4$ for 3 concentrations of Ho^{3+} ions: $x = 0.018$,$x = 0.045$ and $x = 0.080$. The solid curve is the non-interacting specific heat calculated in Section 6.2.

where such a subtraction was also done [1, 3].

The remaining specific heat ΔC is, for all three samples, a broad peak which is shown in Figure 8.3. The crystal grower supplied us with nominally 2%, 4.5% and 8% Ho samples, but the magnitude of the 2% sample was found to be under the curve $C_{\rm SI}$ at higher temperatures ~ 0.8 K. At these temperatures, well above the interaction strengths in the system, the specific heat ΔC should go as T^{-2}. Thus we found that the 2% sample is likely actually 1.8% holmium. Such a small discrepancy in the stoichiometry is quite difficult to resolve using standard chemical analysis techniques, but since we are dividing by the concentration in the specific heat results, it becomes very important. The 4.5% and 8.0% samples were found, by this analysis, to have the same stoichiometry that was quoted by the crystal provider.

With decreasing concentration x the height of this curve is reduced. The peak position $T_{\rm peak}$ is largely independent of x however. There is some variation in $T_{\rm peak}$ but the noise in the measurement (amplified by the subtraction of the single-ion specific heat) makes it difficult to determine exactly. Certainly it does not appear to scale with x as does the peak height.

The broad features observed are somewhat consistent with a spin glass state (which is what was classically expected for this range of stoichiometry). In a spin glass, the critical exponent α is often quite negative (in the range -2 to -4) so there is no sharp feature observed in the specific heat at the spin glass transition [28]. Instead, the specific heat is more indicative of excitations above the ground state of the system. This can be understood with the many valley picture of a spin glass where the system is resting in a local minimum of a very complicated free energy surface (sketched in Figure 8.4). In each of these local minima there may be a ground state as well as excited states which may be occupied more often as the temperature is raised. The simplest model for the specific heat is based on the idea of many nearly-degenerate ground states and also many nearly-degenerate excited states. These excited energy states all have an energy of roughly E_1 and will have a degeneracy n with respect to the, already large, ground state degeneracy. Then the specific heat is given by

$$\Delta C = C_0 \frac{n(E_1/k_BT)^2 e^{-E_1/k_BT}}{(1 - ne^{-E_1/k_BT})^2}. \tag{8.2}$$

This form of the specific heat has been used to fit the data in Figure 8.3 with reasonably good agreement. The fitting parameters are given in Table 8.1. There is no noticeable trend in the parameters C_0,E_1 and n as a function of x. This is likely because the uncertainty on these parameters is quite large – a 2-parameter fit is not adequate to fit the data, but 3 parameters are too many. It is more informative to parameterize the curves by their width and position in temperature.

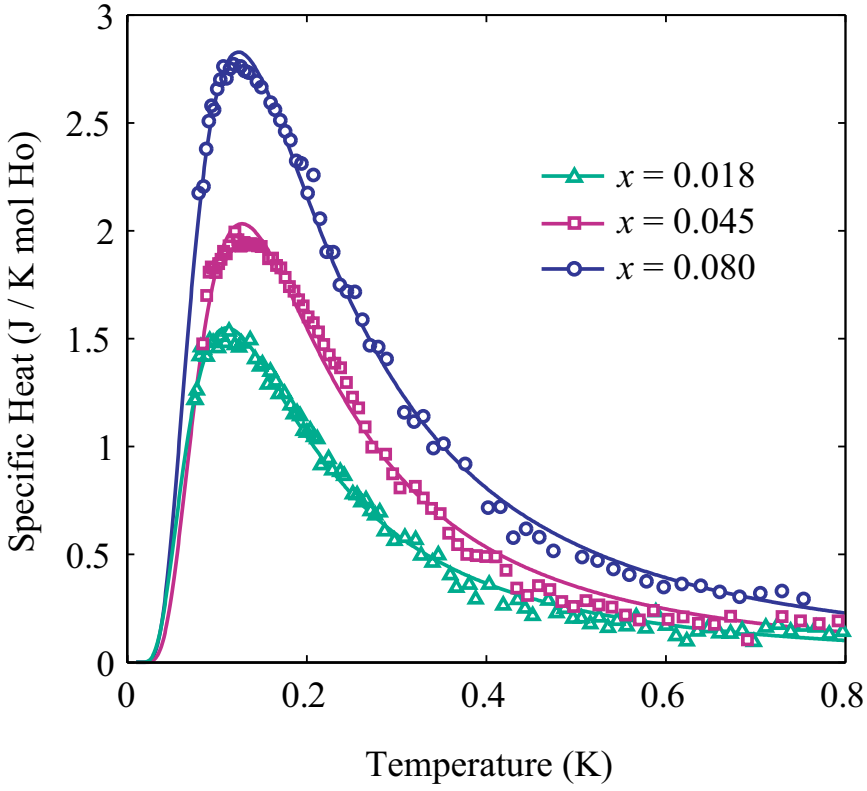

Figure 8.3: The specific heat of $LiHo_xY_{1-x}F_4$ for $x = 0.018, 0.045$ and 0.080 after subtraction of the calculated single-ion specific heat (shown as the solid curve in Figure 8.2). The solid lines are fits of the form of Equation (8.2). The resulting fit parameters are shown in Table 8.1.

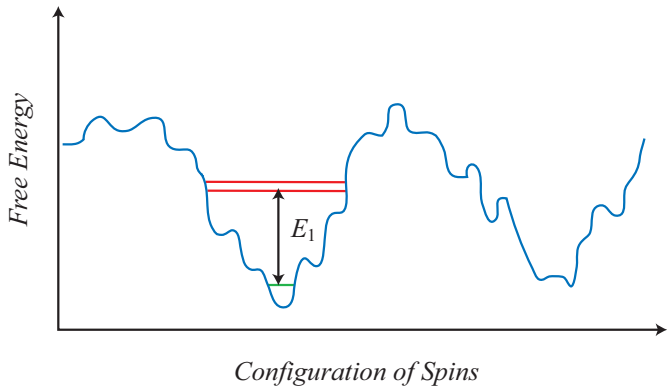

Figure 8.4: A sketch of the complicated free energy landscape of a spin glass which contains many mountains and valleys. The specific heat comes largely from the excited states within one of these valleys.

Parameter	1.8% sample	4.5% sample	8.0% sample	16.7% sample [1]
C_0 (J/K mol Ho)	4.06	3.45	7.31	2.85
E_1/k_B (K)	0.26	0.32	0.29	0.46
n	0.85	1.43	0.86	1.89
T_{peak} (K)	0.11	0.13	0.12	0.17
FWHM/T_{peak}	1.7	1.6	1.7	1.5
S_0/R	0.31	0.21	0.00	0.18

Table 8.1: Fitting parameters used for the subtracted specific heat ΔC as well as the residual entropy and other parameters. Parameters for a 16.7% sample measured by Reich *et al.* [1] are also included.

8.2.2 Entropy

The thermodynamic identity

$$S(T) = \int_0^\infty \frac{C(T)}{T} dT = \int_{-\infty}^\infty C(T) d(\ln T) \tag{8.3}$$

may be used to obtain the entropy that has been released from the system at a given temperature. The total, high-temperature entropy of an Ising system is $R \ln 2$. One would typically expect to obtain this amount of entropy in numerically integrating C/T, but in frustrated magnetic systems there is often a large number of degenerate ground states and so a residual entropy S_0 may be observed at zero T.

Our measurements obviously cannot extend to zero temperature, so we should not expect to pick up all of the entropy in the system. Typically in spin glasses, the specific heat is seen to behave linearly in temperature below the maximum in the curve [31, 81] in keeping with Anderson's two-level system (TLS) argument [30]. Thus we have done a linear extrapolation to zero temperature before numerically integrating. The extrapolation was done by taking the fits of Equation (8.2) to the data and connecting the fits to a linear term at low temperature such that the resulting curves are smooth. These curves are shown as the solid lines in Figure 8.5, extended to zero temperature. The integral was done numerically over the data and at lower temperatures, the extrapolated linear term becomes a linear part of the entropy as well.

The results of the numerical integral are shown in Figure 8.6. The data has been shifted so that it tends towards $R \ln 2$ at the high temperatures. The residual entropy as a function of concentration $S_0(x)$ is shown in the inset of Figure 8.6. With decreasing x, the residual entropy in the system is found to get larger, suggesting that there is a larger number of degenerate ground states. With the linear assumption, the 8% sample has essentially zero residual entropy. The 4.5% sample has a residual entropy of $0.21R$ which is quite close to $0.199R$ which is the amount of residual entropy predicted for the SK model of a spin glass [82] and so is not a surprising amount of residual entropy to be found in a glassy system. The 1.8% sample is found to have a larger residual entropy per mole of Ho at $0.31R$.

Snider *et al.* [4] have performed Monte-Carlo simulations on the dilute, dipolar-coupled Ising model on a simple cubic lattice and they have found a concentration $x_c \simeq 0.20$ at which point the spin glass ordering ceases in conjunction with the residual entropy dropping to zero. Below this point, the system is a spin liquid and the residual entropy increases with decreasing concentration. The Monte Carlo data is shown in Figure 4.2. Our entropy data seems to be consistent with this picture with two discrepancies. First, our residual entropy is much larger than predicted by the numerical simulations: for the $x = 0.045$

sample Snider *et al.* predict $S_0 \simeq 0.067$ J / K mol Ho where we have measured (assuming a linear behaviour at low T) $S_0 \simeq 1.7$ J/K mol Ho. Second,the point at which $S_0 = 0$ is closer to $x = 0.080$ where the Monte Carlo simulations find $S_0 = 0$ at $x \simeq 0.2$. The simulations, however, were not performed on the same crystal lattice as $LiHo_xY_{1-x}F_4$ and terms in the Hamiltonian that would detract from the Ising character of the system (such as the nuclear hyperfine interaction) were not taken into account. It is possible that there is much more frustration in the real lattice than in a simple cubic lattice leading to a higher ground state entropy. However, typically such residual entropy requires many degenerate ground states which result from increased symmetry rather than more complexity in the system. The nuclear moments which were ignored in the simulation and possess many degrees of freedom, could also hold much of that residual entropy observed in experiment.

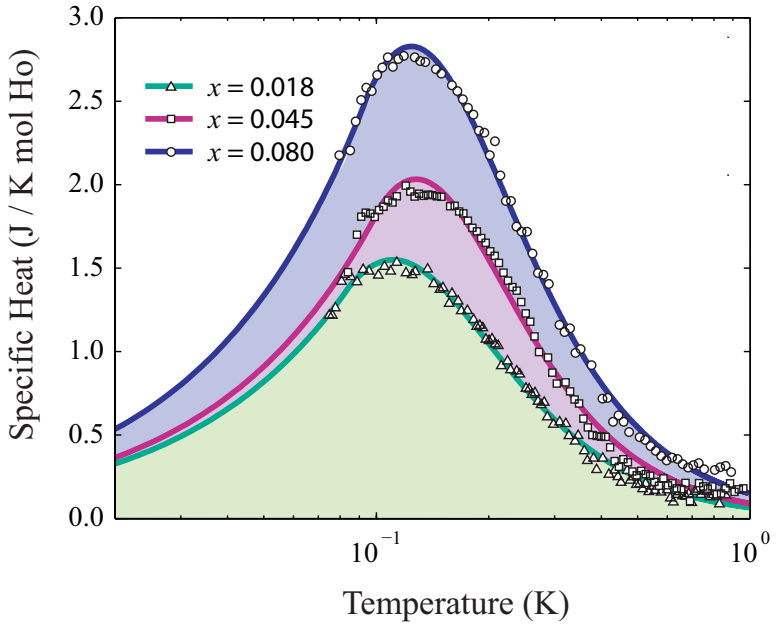

Figure 8.5: The subtracted specific heat (open symbols) with fit and linear extrapolation to 0 temperature (solid lines) for three values of x. Here we plot the temperature on a log scale so the shaded area under the curves is proportional to the entropy in the system.

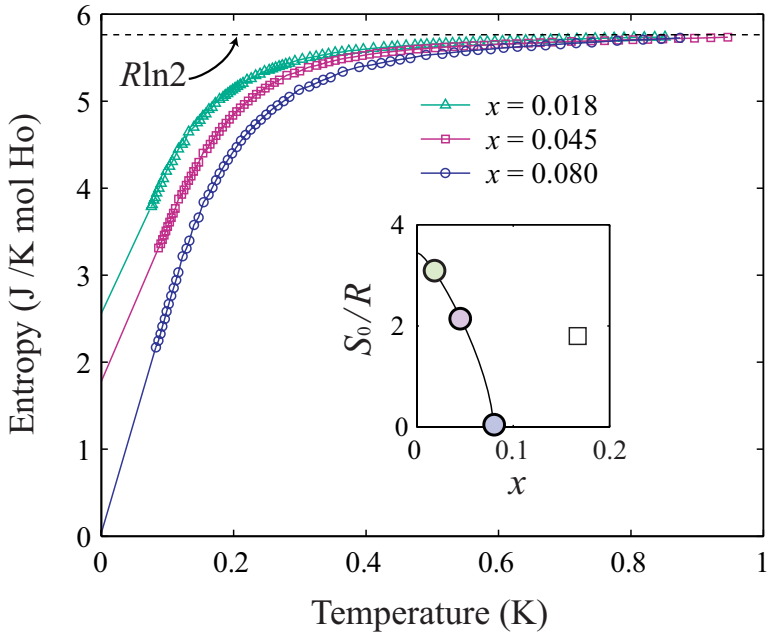

Figure 8.6: The entropy in the system as a function of temperature. The high temperature entropy is shifted to match with $R \ln 2$. The entropy at 0 K is therefore the residual entropy in the system S_0 assuming a linear temperature dependence of the specific heat below the maximum. The inset shows the residual entropy as a function of Ho concentration (x). The solid, black line is a guide to the eye. The residual entropy of a 16.7% sample measured by Reich *et al.* [1] is the open square.

8.2.3 Comparison with Previous Measurements

As can be seen in Figure 8.7, our specific heat measurement of $LiHo_{0.045}Y_{0.955}F_4$ differs significantly from a previous measurement of the same stoichiometry shown as the open, black squares [1, 3]. The two data sets agree in a range of temperatures from $\sim$ 300 mK to $\sim$ 800 mK, but below and above that range, there is a very large discrepancy. The previous measurement drops away quickly at 300 mK resulting in a sharp feature. There is another peak seen at around 110 mK. Our measurement, on the other hand, shows no sharp peaks, but instead shows a broad feature which is more consistent with a spin glass. Above 800 mK, the previous measurement shows an increase in the heat capacity which cannot be explained by phonons or higher crystal field energy levels. In our measurement, in this range, the specific heat is decaying roughly as T^{-2} as would be expected in a temperature range well above the scale of the interactions in the system. Thermal conductivity measurements of a 4% sample also did not show any sharp features at 110 and 300 mK [76].

The very small heat capacity of the previous measurement implies that there is very little entropy released – only about 15% of the total expected entropy of an Ising system ($R \ln 2$). Our measurement accounts for a much more reasonable amount of entropy – roughly 43% over the temperature range studied or 70% if the specific heat is extrapolated linearly to zero temperature. As stated previously, in our measurement this leaves a residual entropy of $0.21R$ which is very reasonable as it is close to what is expected for certain spin glass models [82].

The reason for the discrepancy between data sets is not known at this time, though we may propose several possible explanations. First of all, one might think that an error in the stoichiometry of the sample could lead to a miscalculation of the specific heat and after subtracting the nuclear term, this could lead to a very unusual shape of curve. However, the fact that the data sets agree between 300 mK and 800 mK would suggest that the stoichiometries of the two samples are the same and likely both correct at 4.5% holmium.

Sample quality could alter the form of the specific heat in two principal ways. The first way in which the sample quality could adversely effect the specific heat is through crystal strain. If there is significant distortion of the crystal lattice, the crystal field surrounding the Ho^{3+} ions would be altered. As is demonstrated in Section 6.3, a gradient in the crystal strain would lead to a drop in the non-interacting specific heat between 100 mK and 600 mK and a rise in the specific heat above 600 mK. It is possible that such a sample quality problem could explain the anomalously low specific heat measured by Ghosh *et al.* [3].

The simulations done in Section 6.3 using a Gaussian distribution of B_2^2 crystal field parameters are not able to generate the sharp features that were observed previously, but it might still be possible using a more complicated distribution of lattice distortions

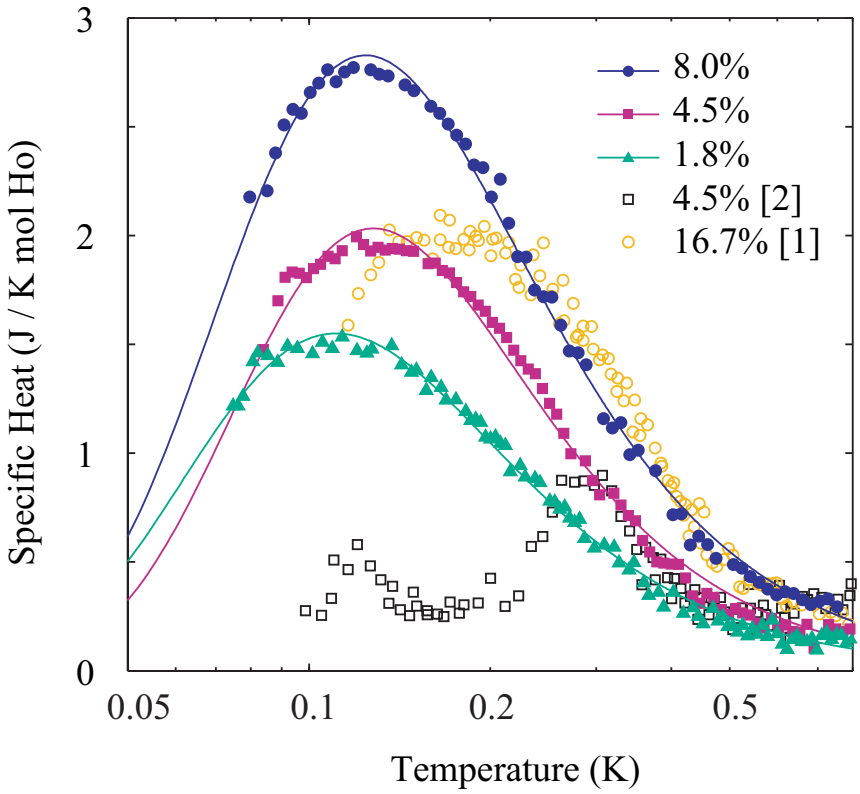

Figure 8.7: Comparison of the subtracted specific heat data from this work and from previous measurements. The open, black squares are from an $x = 0.045$ sample measured by Ghosh *et al.* [3] and the open, gold circles are from an $x = 0.167$, spin glass sample measured by Reich *et al.* [1].

and including the effects of strain on higher-order crystal field parameters. But if one simply looks at the magnitude of effect required, a change in the lattice parameter of 0.2 Å between adjacent unit cells could be sufficient. This corresponds to a very large amount of strain and therefore very bad sample quality and thus seems unlikely. If crystal strain is the answer to this difference, our samples must be of higher quality as the existence of a large amount of strain in our samples would imply that the interacting part of the specific heat ΔC would be larger. This would likely mean that the total entropy in our system is larger than $R \ln 2$ which is not physically possible. Additionally, X-ray experiments on our samples have demonstrated that the sample quality is extremely high and surely would not contain enough distortion to cause any noticeable change in the specific heat.

The second way in which sample quality could effect this measurement, or all the exciting physics in this system for that matter, is in the distribution of Ho^{3+} moments. It is not so clear how this would effect the specific heat, but it is probable that clustering of the Ho^{3+} ions, rather than the expected random distribution, could significantly alter the magnetic order and therefore the specific heat in the system. It is possible that largely isolated clusters of Ho moments could develop order at a specific temperature in conjunction with the peaks in ΔC observed by Ghosh *et al.* [3]. The remainder of the moments would then, in some sense, be much more dilute and would not tend to exhibit any collective behaviour until much lower temperatures. The model presented by Ghosh *et al.* [3], which reproduced their experiment to some degree, is largely concerned with the more energetic interactions of nearby moments and does not emphasize the long-range nature of the dipolar interaction. Such a picture would be more consistent with physical clustering of the spins. This might also account for their observation of coherent oscillations of clusters of ~ 260 Ho^{3+} ions [2].

A final possible explanation for the discrepancy is simply an error in experiment. We have been extremely careful in analyzing our experimental apparatus and accounting for all the heat flow in the system. As such, we are confident that our results are correct to within a much smaller error than would be required to reproduce the data of Ghosh *et al.* [3]. Additionally, the chances of error in our experiment smoothing out sharp peaks at 110 and 300 mK is very small. Calibration errors, for example, can alter the specific heat by a certain amount, but one would not expect these errors to, by chance, line up perfectly with and counteract the peaks in the conflicting data set. Also important to note is the fact that our data from three different concentrations are similar and show a consistent trend. The opposing data were obtained via a similar experimental technique, though all components were fixed to a substrate. As was discussed in Section 7.4.5, a substrate can lead to an overestimate of the heat capacity of the sample – not the other way around. Significant decoupling of the thermometer from the substrate, on the other hand, could lead to an overestimation of the temperature change ΔT and thus an underestimation of

C. It is difficult, nonetheless, to see how such a decoupling could lead to the sharp peaks seen in their data [3].

8.2.4 Comparison with Spin Glass Literature

As was mentioned previously, our measurements of the specific heat are somewhat consistent with the specific heat of a spin glass largely because it shows a broad maximum with no sharp peaks. The data taken on these three samples looks qualitatively much more like the specific heat measured for an $x = 0.167$ sample [1] which is also shown in Figure 8.7 as the open, gold circles than a previous measurement of an $x = 0.045$ sample [3]. The 16.7% sample was studied with ac susceptibility and nonlinear susceptibility and was shown conclusively to be a spin glass [1, 9, 10] with an ordering temperature of around 0.13 K. It shows a maximum in its specific heat at about 0.17 K.

An effective way of parameterizing the width of the feature is to take the full width at half maximum (FWHM) divided by the peak temperature T_{peak}. This parameter is listed in Table 8.1 for these three samples and the 16.7% which was previously measured. In our measurements it generally has a value around 1.7 and in the 16.7% sample it is roughly 1.5. This parameter was found to be approximately 1.2 in the metallic spin glass Au*Fe* [81] and approximately 1.5 for the insulting spin glass $Eu_xSr_{1-x}S$ [83]. Thus our specific heat curves appear to be even slightly broader than is conventionally seen in spin glasses.

A general rule of thumb is that the peak in ΔC of spin glasses is found to be roughly 20% higher than the spin glass transition temperature [45]. This also seems to apply, roughly, to 16.7% Ho:YLF [1, 9, 10]. In our measurements, the peak temperature is very similar for all three samples, from 0.11 K to 0.13 K. The 20% rule would therefore imply spin glass transitions of 98 mK to 108 mK. Thus the spin glass transition would seem not to scale significantly with the concentration x. From the theory of Stephen and Aharony [12] however, one would expect the spin glass transition temperature to vary roughly linearly with x in this regime. This rule of thumb may not be entirely valid, however, as the spin glass transition temperatures to which T_{peak} was compared, were simply obtained from the cusp in a 'low' frequency measurement rather than through a more elaborate dynamical scaling analysis [45].

Another trend, previously observed in spin glasses [84] is that the specific heat for different concentrations observes the following law

$$\frac{\Delta C(T,h,x)}{x} = f\left(\frac{T}{x}, \frac{h}{x}\right). \tag{8.4}$$

Though the magnitudes of the specific heat (normalized by x) for these three samples are

similar, the temperature dependence does not at all scale with x and this law does not hold here.

Thus there are significant differences between these measurements and those of classic spin glasses. The fact that our measured specific heat is a broad feature is not enough to say that it is a spin glass and not an 'anti-glass' or spin liquid. The specific heat of $Eu_xSr_{1-x}S$ below the percolation threshold in the super-paramagnetic regime is also a broad feature despite not being a spin glass [85].

Possibly, the most important indication of a spin glass state in the heat capacity is a linear behaviour at low temperature. Thus far, we have only presented higher temperature data where such a trend could not be observed, but in the next section some tentative low temperature behaviour will be discussed.

8.2.5 Low Temperature Limit

The initial discovery of spin glasses stemmed from the observation of an anomalous linear specific heat at low temperatures in alloys such as Cu*Mn*. As was discussed in Section 3.1, the explanation for this behaviour, proposed by Anderson [30], is based on a collection of two level systems (TLS's) with a distribution of energies and therefore tunneling rates. This is a phenomenological explanation for the linear specific heat and other theories predict different low temperature limits [86]. Nevertheless, most measurements of the specific heat of spin glasses have seen a largely linear specific heat with some higher order corrections [31, 34, 83]. Careful measurements of Cu*Mn* show that ΔC is not in fact linear at low temperatures [87]. There is a range where the specific heat is a straight line as a function of temperature, but at lower temperatures (around 1 K) it begins to deviate from that line and appears to approach zero quadratically.

Our low-temperature data is limited at this point in time and obtaining good thermometer calibrations below 100 mK can be very difficult because of self-heating and other factors which were discussed in Section 7.4.6. Some results for the specific heat below the maximum are shown in Figure 8.8. The linear extrapolations used for the entropy calculation are shown as the dashed lines and are reasonably good fits to the data above 60 mK. It is impossible given the error in the measurement, at this time, to conclude whether the low-temperature behaviour is linear or steeper than linear. Though the data sit below the linear extrapolations at lower temperatures, a not unlikely 5 mK self-heating at 50 mK could lead to an almost perfect linear behaviour (open symbols). Note that the thermal conductivity of the alumina thermometer substrate and the conductivity of the boundary between solids will increase as T^3 [78]. The heat load should be roughly independent of temperature so this means that above $\sim$ 75 mK there will be an insignificant change in temperature caused by self-heating.

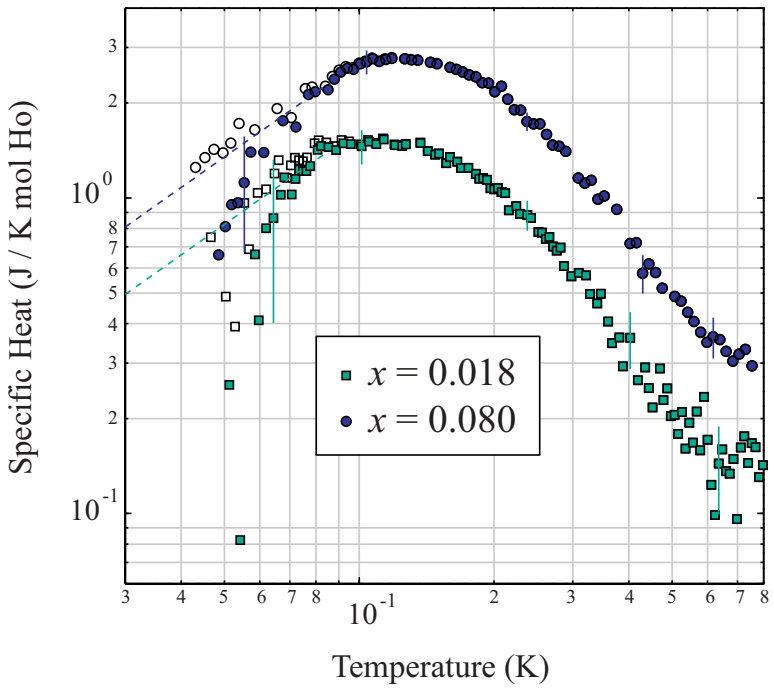

Figure 8.8: A log-log plot showing the low-temperature behaviour of the specific heat for the 1.8% and 8.0% samples (filled symbols). The dashed lines are the linear extrapolation used for the entropy integral. The data is seen to deviate from the linear extrapolation at low T, but the estimated systematic error is quite large at this point (as shown by the vertical lines). If there is 5 mK of self-heating at 50 mK (as is discussed in Section 7.4.6) then the open symbols apply. Thus if there is significant self-heating in the system the low-temperature behaviour can significantly skewed.

It may be possible that this low concentration regime, in which the "anti-glass" physics are observed, may not display the linear $\Delta C(T)$ which is expected for spin glasses. In the material $Eu_xSr_{1-x}S$, for concentrations below the percolation threshold $x_C \simeq 0.13$ in the super-paramagnetic regime, the specific heat is still a broad feature but it has an exponential rise at low temperatures instead of the linear specific heat seen above the percolation threshold [85]. It is also interesting to note that in structural glasses doped with rare-earth ions, magnetic tunneling states (which are the quantities expected to give rise to the linear specific heat) were found with Dy ions (Kramers ions) but not with Ho ions (non-Kramers ions) [88]. Thus it may be possible that even in the spin glass regime of $LiHo_xY_{1-x}F_4$, a linear specific heat may not be observed.

It would be valuable to continue a more careful study of the low-T specific heat of these samples and of samples that are clearly in the spin glass regime. It is, however, an extremely challenging measurement. Even without any errors in calibration or due to self-heating, it is difficult to be certain of the exact form of the non-interacting specific heat which must be subtracted. It may be necessary to go to much lower temperatures where the nuclear component is much less significant in order to make such a determination.

8.3 Thermal Relaxation at Low Temperatures

During heat capacity measurements, some unusual behaviour of the sample temperature was noticed. At low temperatures (below 100 mK), while heat is being applied through the heater, the thermometer temperature gets quite high. When the heater is switched off, the thermometer temperature shows several distinct time constants of relaxation. There is the very long time constant $\tau_{WL} = C/K_{WL}$ of more than an hour which is chosen when designing the apparatus. This time constant is so long that this part of the temperature relaxation appears linear over the period of time that is measured. There are some fairly quick time constants which likely come from a time constant inherent in the thermometer and/or reduced thermal conductivity of the sample at low temperatures. There is, however, a much more interesting and abnormally long temperature relaxation observed at these temperatures.

At the start of the heat pulse the thermometer rises much higher than would be expected given the sample's heat capacity and after the heater is shut off, appears to fall over a period of several minutes to what would normally be considered the sample temperature. This is shown in the inset of Figure 8.10. If we were employing a substrate in our measurement this effect would be expected due to decoupling of the substrate from the sample. However, we are not using a substrate and this effect cannot come from decoupling of the thermometer from the sample.

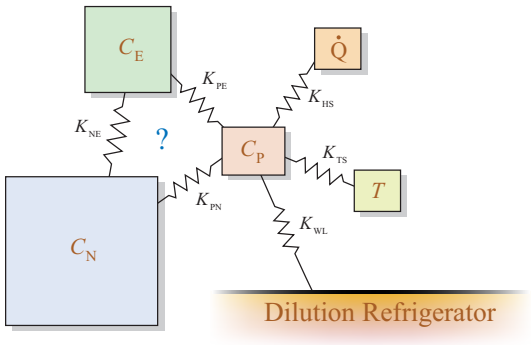

Figure 8.9: A schematic diagram of the various heat capacities and thermal connections in the system. The connections between the nuclear moments and the phonons or the nuclear moments and the electrons are proposed as the cause of the slow thermal relaxation observed in experiment. The boxes labeled $\dot{Q}$ and T are the heater and thermometer respectively. The details of how the various components are connected is not known at this time.

The only explanation is that it comes from slow relaxation within the sample. A likely mechanism for this relaxation is from the thermal connections between different contributions to the heat capacity of the sample. The sample's specific heat consists of several distinct parts: the nuclear specific heat C_N, the electronic specific heat from the interactions between moments C_E and the phonon or lattice specific heat C_P. Since the sample is an insulator, the only mechanism of sharing heat between it and the thermometer is through phonons. Thus the thermometer measures the temperature of the phonons T_P and not the temperature of the nuclear moments T_N or electronic moments T_E. Most likely, there is a long spin-lattice relaxation between the phonons (which have a relatively small heat capacity) and the nuclear moments (which have most of the heat capacity in the system). Such a slow spin-lattice relaxation has been observed in specific heat measurements in other systems [89]. During the heat pulse, there is a temperature difference between the lattice and the nuclear moments. After the heating is shut off, the temperatures slowly equilibrate. It is difficult to say how the electronic moments should be thermally connected in this system. They are strongly coupled to the nuclear moments through the hyperfine interaction and are likely coupled to the lattice via the crystal field energy. A diagram of the relevant heat capacities and thermal links is shown in Figure 8.9.

Below about 80 mK, this effect is very significant and was observed in the $x = 0.018$ and $x = 0.080$ samples (there is a lack of low temperature data for the $x = 0.045$ sample). The temperature relaxations for the $x = 0.018$ sample are plotted in Figure 8.10. The

effect becomes more difficult to discern above 80 mK, though there are some indications that it is still happening up to about 110 mK in all three samples.

We have described these temperature relaxations by their time constant, but in fact they are not well fit by an exponential function. The drop in temperature is too steep near the beginning and too shallow later on in time for it to be described by one exponential time constant. Multiple time constants of relaxation yield better fits, as do stretched exponentials of the form

$$T(t) \propto \exp[-(t/\tau)^{\beta}] \tag{8.5}$$

with $\beta \sim 0.75$.

The effect seems to disappear rather quickly around 80 mK which implies that the thermal connection K_{NP} is strongly temperature dependent. This could also explain the need for a stretched exponential to fit the temperature relaxation as a simple exponential decay requires $C/\kappa = \tau$ to be fairly temperature independent.

For some pulses, at different temperatures, but with the same power $\dot{Q}$, the temperature rise during the pulse is actually larger at lower temperatures. Better controlled experiments must be performed in this temperature range in order to understand the dependence of this effect on the heater power, sample temperature, waiting time between pulse, etc.

One alternative explanation for this long temperature relaxation could come from the glassy state of the electronic moments. In true, structural glasses, a frequency-dependent specific heat has been observed [79]. Their experiments are done using an ac heat capacity measurement where the heater power is oscillated at a frequency f and the amplitude and phase of the sample's temperature oscillations is measured. As with ac susceptibility, this gives an in-phase component $C'(f,T)$ and an out-of-phase component $C''(f,T)$. The results have a frequency dependence very similar to that seen in the ac susceptibility of spin glasses or the dielectric susceptibility of structural glasses. The peak position of the out-of-phase component $f_p(T)$ was found to obey a Fulcher law (see Section 3.1). The shape of the curve of $C''(f)$ was fit well by the William-Watts distribution which is the Fourier transform of the stretched exponential given in equation (8.5) with $\beta \simeq 0.65$. This is close to $\beta \simeq 0.75$ which was obtained in fits of our temperature relaxation data to a stretched exponential.

Reich *et al.* also observed a slower than exponential temperature relaxation in a 4.5% sample below 100 mK [1]. Their analysis of this relaxation, however, was done on a comparable time scale to the characteristic time constant of the weak link in their specific heat measurement. They did observe a smaller, quicker temperature relaxation just after a heat pulse in a window of around 100 s. This is more likely to be the same effect that we have observed, though their use of a substrate likely makes it a much smaller temperature change. They attributed this to decoupling of the thermometer from the sample.

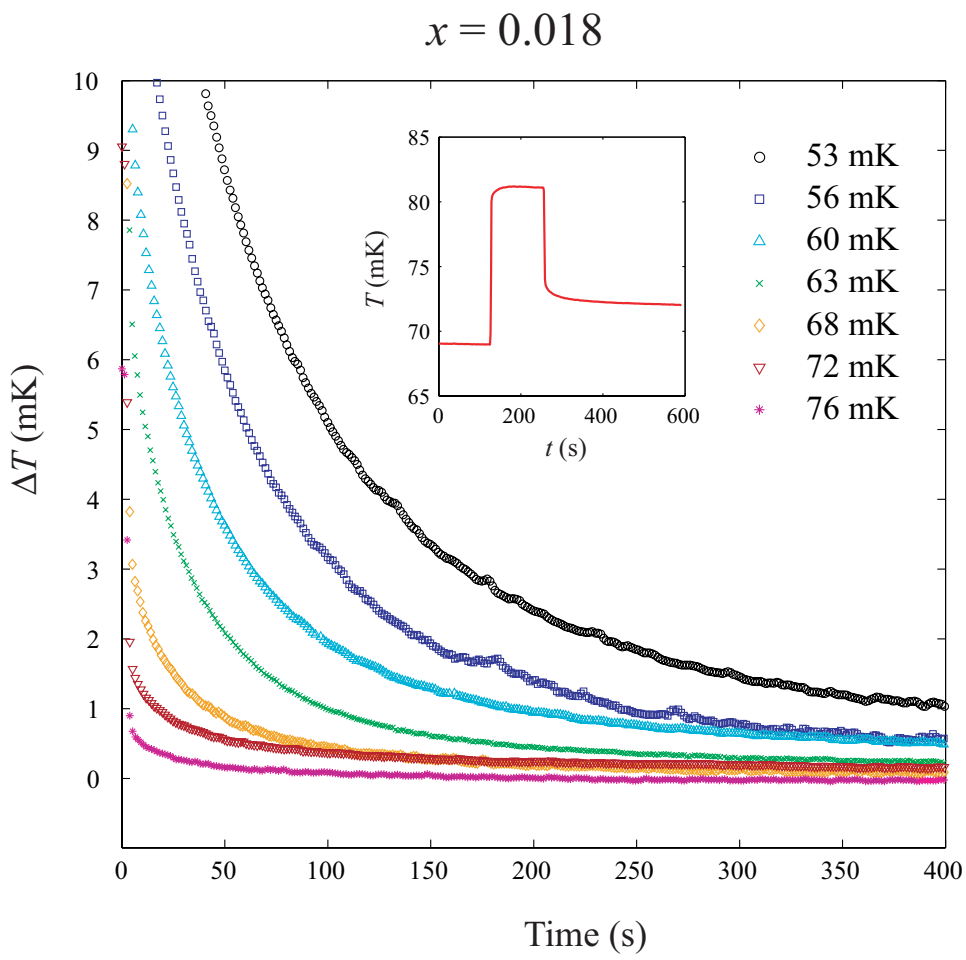

Figure 8.10: The slow thermal relaxation of the $x = 0.018$ sample plotted for different final temperatures. The approximately linear decay due to the long time constant of the weak link has been subtracted away. The resulting form is not well fit by an ordinary exponential. Using two different time constants or a stretched exponential form $\exp\left[-(t/\tau)^{\beta}\right]$ give better results, but still do not adequately fit the data. The inset shows a heat pulse at low temperatures – the slow thermal relaxation is seen on the rise at the beginning of the heat pulse as well as on the fall after the heat pulse.

Chapter 9

Conclusion

We have very carefully measured the specific heat of several samples from the series $LiHo_xY_{1-x}F_4$. More specifically, we have studied 1.8%, 4.5% and 8.0% holmium concentrations which are at and around the concentration at which previous work has observed a very unexpected and exciting spin liquid or "anti-glass" state [1, 2]. Most importantly, our measurements have not reproduced the sharp features in specific heat that were observed previously [3].

Instead, after subtraction of a calculated non-interacting specific heat, we observe a broad maximum in all three samples studied. This feature is in some ways consistent with a spin glass and other ways not. A spin glass is expected to be a broad feature with no pronounced anomalies at the freezing transition and a roughly linear specific heat below the maximum. The measured specific heat is indeed broad with no sharp peaks. The low temperature behaviour seems to be steeper than linear, but the error bars on our measurement in that regime are currently too large to conclusively rule out a linear temperature dependence. The position of the maximum in the specific heat T_{peak} does not scale with x and is nearly equal for the three concentrations studied, contrary to what one would expect for a spin glass.

If we numerically integrate $\Delta C/T$ (after assuming a linear temperature dependence below the maximum) we can extract the residual entropy S_0. This quantity is found to be close to zero for the 8.0% compound and increases with decreasing concentration. This is consistent with recent Monte Carlo simulations [4] of dipolar-coupled Ising moments which find no spin glass ordering below a certain concentration x_c despite the previous expectation that there should be no percolation threshold [12]. These simulations also predict a smooth 'bump' in the specific heat, even in the spin liquid state.

Based on the data and the numerical simulations, we suggest that it is indeed possible that there is a spin liquid state below a certain concentration x_c and that this critical

concentration is near $x = 0.080$. If it exists, however, this spin liquid state does not express itself as sharp features in the specific heat as was observed previously. We have been extremely careful in ruling out experimental errors and our samples have been found to be very high quality. Our results are also much more plausible as we observe the release of 70 to 100% of the total entropy in the system (leaving a residual entropy which is close to what has been theoretically calculated for spin glasses) where previous measurements only picked up 15% of $R \ln 2$. As was discussed in Section 6.3, poor sample quality could lead to a lowering of the non-interacting specific heat which would be seen as an apparent dip in ΔC.

Also in these three samples of low holmium concentration, we have observed a slow relaxation of the sample temperature at temperatures below around 80 mK. This effect cannot be fit with a single time constant of relaxation, but is better approximated by a stretched exponential. Possible explanations are a slow spin-lattice relaxation or an effect due to relaxation of the glassy state of the material. The latter is supported by the slower than exponential relaxation which has been observed in structural glasses [79].

In this work, we have also measured the ac susceptibility as a function of temperature of a 45% Ho sample and find that it exhibits a paramagnetic to ferromagnetic transition at 0.68 K in keeping with previous measurements [1].

9.1 Future Work

The specific heat measurements on these samples are not conclusive about the nature of this low concentration regime. The true test for the existence of the "anti-glass" state must be the frequency-dependent ac susceptibility of the samples. We have built a very sensitive SQUID magnetometer which is capable of dc measurements and ac measurements with a flat frequency response below 10 kHz. Measuring $\chi''(f)$ on these three samples as well as 12% and 25% Ho samples will hopefully give a clear picture of the existence and range of the spin liquid state.

It would also be interesting to further explore the specific heat and slow thermal relaxation of these samples. More in depth measurements at lower temperatures could be performed in order to determine exactly the low-temperature behaviour. A change from linear to some other temperature dependence might signal a change from spin glass to "anti-glass" for example. Better controlled experiments to observe the thermal relaxation should also be performed as we have too small a data set currently in order to make strong conclusions about the origin of this effect.

Bibliography

[1] D. H. Reich *et al.*, Phys. Rev. B **42**, 4631 (1990).

[2] S. Ghosh, R. Parthasarathy, T. Rosenbaum, and G. Aeppli, Science **296**, 2195 (2002).

[3] S. Ghosh, T. Rosenbaum, G. Aeppli, and S. Coppersmith, Nature **425**, 48 (2003).

[4] J. Snider and C. C. Yu, Phys. Rev. B **72**, 214203 (2005).

[5] J. A. Griffin, M. Huster, and R. J. Folweiler, Phys. Rev. B **22**, 4370 (1980).

[6] D. Bitko, T. F. Rosenbaum, and G. Aeppli, Phys. Rev. Lett. **77**, 940 (1996).

[7] J. Brooke, D. Bitko, T. F. Rosenbaum, and G. Aeppli, Science **284**, 779 (1999).

[8] J. Brooke, T. F. Rosenbaum, and G. Aeppli, Nature **413**, 610 (2001).

[9] W. Wu, B. Ellman, T. F. Rosenbaum, G. Aeppli, and D. H. Reich, Phys. Rev. Lett. **67**, 2076 (1991).

[10] W. Wu, D. Bitko, T. F. Rosenbaum, and G. Aeppli, Phys. Rev. Lett. **71**, 1919192 (1993).

[11] S. Ghosh, *Non-Linear Dynamics in Spin Liquids*, PhD thesis, The University of Chicago, 2003.

[12] M. J. Stephen and A. Aharony, J. Phys. C **14**, 1665 (1981).

[13] M. T. Hutchings, Solid State Phys. **16**, 227 (1964).

[14] K. W. H. Stevens, Proc. Phys. Soc. A **65**, 209 (1952).

[15] P. B. Chakraborty, P. Henelius, H. Kjønsberg, A. W. Sandvik, and S. M. Girvin, Phys. Rev. B **70**, 144411 (2004).

[16] R. Giraud, W. Wernsdorfer, A. M. Tkachuk, D. Mailly, and B. Barbara, Phys. Rev. Lett. **87**, 057203 (2001).

[17] P. E. Hansen, T. Johansson, and R. Nevald, Phys. Rev. B **12**, 5315 (1975).

[18] N. Karayianis, D. E. Wortman, and H. P. Jenssen, J. Phys. Chem. Solids **37**, 675 (1976).

[19] B. M. Walsh, G. Grew, and N. P. Barnes, J. Phys.: Condens. Mater. **17**, 7643 (2005).

[20] A. Abragam and B. Bleaney, *Electron Paramagnetic Resonance of Transition Ions* (Clarendon Press, Oxford, 1970).

[21] J. Magariño, J. Tuchendler, J. P. D'Haenens, and A. Linz, Phys. Rev. B **21**, 18 (1980).

[22] J. Magariño, J. Tuchendler, J. P. D'Haenens, and A. Linz, Phys. Rev. B **13**, 2805 (1976).

[23] G. Mennenga, L. de Jongh, and W. Huiskamp, J. Magn. Magn. Mater. **44**, 59 (1984).

[24] S. Sachdev, *Quantum Phase Transitions* (Cambridge University Press, 1999).

[25] A. P. Ramirez, A. Hayashi, R. J. Cava, R. Siddharthan, and B. S. Shastry, Nature **399**, 333 (1999).

[26] B. C. den Hertog and M. J. P. Gingras, Phys. Rev. Lett. **84**, 3430 (2000).

[27] P. Schiffer *et al.*, Physical Review Letters **74**, 2379 (1995).

[28] K. H. Fischer and J. A. Hertz, *Spin Glasses* (Cambridge University Press, 1991).

[29] J. de Nobel and F. J. du Chatenier, Physica **25**, 969 (1959).

[30] P. W. Anderson, B. I. Halperin, and C. M. Varma, Philosophical Magazine **25**, 1 (1972).

[31] L. E. Wenger and P. H. Keesom, Physical Review B **13**, 4053 (1976).

[32] A. T. Ogielski, Physical Review B **32**, 7384 (1985).

[33] W. E. Fogle, J. D. Boyer, R. A. Fisher, and N. E. Phillips, Physical Review Letters **50**, 1815 (1983).

[34] D. L. Martin, Phys. Rev. B **21**, 1902 (1980).

[35] G. E. Brodale, R. A. Fisher, W. E. Fogle, N. E. Phillips, and J. V. Curen, J. Magn. Magn. Mater. **31-34**, 1331 (1983).

[36] V. Cannella, J. A. Mydosh, and J. I. Budnick, J. Appl. Phys. **42**, 1689 (1971).

[37] V. Cannella and J. A. Mydosh, Phys. Rev. B **6**, 4220 (1972).

[38] J. L. Tholence, Solid State Commun. **35**, 113 (1980).

[39] C. A. M. Mulder, A. J. van Duyneveldt, and J. A. Mydosh, Phys. Rev. B **23**, 1384 (1981).

[40] C. A. M. Mulder, A. J. van Duyneveldt, and J. A. Mydosh, Phys. Rev. B **25**, 515 (1982).

[41] J. Ferré and J. Rajchenbach, J. Appl. Phys. **52**, 1697 (1981).

[42] C. C. Paulsen, S. J. Williamson, and H. Maletta, Phys. Rev. Lett. **59**, 128 (1987).

[43] S. Nagata, P. H. Keesom, and H. R. Harrison, Phys. Rev. B **19**, 1633 (1979).

[44] P. Monod and H. Bouchiat, J. Phys. (Paris) Lett. **43**, L45 (1982).

[45] K. Binder and A. P. Young, Reviews of Modern Physics **58**, 801 (1986).

[46] S. F. Edwards and P. W. Anderson, J. Phys. F **5**, 965 (1975).

[47] D. Sherrington and S. Kirkpatrick, Phys. Rev. Lett. **35**, 1792 (1975).

[48] G. Parisi, Phys. Rev. Lett. **43**, 1754 (1979).

[49] G. Parisi, J. Phys. A **13**, 1887 (1980).

[50] J. W. Essam, *Phase Transitions and Critical Phenomena* (Academic Press Inc., London, 1972), chap. 6, p. 197.

[51] M. J. Stephen and G. S. Grest, Phys. Rev. Lett. **38**, 567 (1977).

[52] W. Kinzel and K. Binder, Phys. Rev. B **24**, 2701 (1981).

[53] A. Aharony, Phys. Rev. B **8**, 3363 (1973).

[54] N. M. Fujiki, K. De'Bell, and D. J. W. Geldart, Phys. Rev. B **36**, 8512 (1987).

[55] G. Eiselt, J. Kotzler, H. Maletta, D. Stauffer, and K. Binder, Phys. Rev. B **19**, 2664 (1979).

[56] H. Maletta and W. Felsch, Phys. Rev. B **20**, 1245 (1979).

[57] J. L. Tholence, J. Appl. Phys. **50**, 7369 (1979).

[58] H. Maletta and P. Convert, Phys. Rev. Lett. **42**, 108 (1979).

[59] R. P. Peters, C. Buchal, M. Kubota, R. M. Mueller, and F. Pobell, Phys. Rev. Lett. **53**, 1108 (1984).

[60] J. J. Folkins, J. A. Griffin, and D. U. Gubser, Phys. Rev. B **25**, 405 (1982).

[61] R. W. Youngblood, G. Aeppli, J. D. Axe, and J. A. Griffin, Phys. Rev. Lett. **49**, 1724 (1982).

[62] D. H. Reich and T. F. Rosenbaum, Phys. Rev. Lett. **59**, 1969 (1987).

[63] K. Kjaer, J. Als-Nielsen, I. Laursen, and F. K. Larsen, J. Phys.: Cond. Mat. **1**, 5743 (1989).

[64] R. Frowein, J. Kötzler, and W. Assmus, Phys. Rev. Lett. **42**, 739 (1979).

[65] P. Beauvillain and J.-P. Renard, Phys. Rev. B **18**, 3360 (1978).

[66] H.-J. Xu, B. Bergersen, and Z. Racz, J. Phys.: Cond. Mat. **4**, 2035 (1992).

[67] M. Suzuki, Prog. Theor. Phys. **56**, 1454 (1976).

[68] D. Bitko, *Order and Disorder in a Model Quantum Magnet*, PhD thesis, University of Chicago, 1997.

[69] J. Brooke, *Quantum Fluctuations and Disorder in a Model Magnet*, PhD thesis, University of Chicago, 2000.

[70] D. Hüser, L. E. Wenger, A. J. van Duyneveldt, and J. A. Mydosh, Phys. Rev. B **27**, 3100 (1983).

[71] D. S. Fisher and D. A. Huse, Phys. Rev. Lett. **56**, 1601 (1986).

[72] M. Schechter and P. C. E. Stamp, Phys. Rev. Lett. **95**, 267208 (2005).

[73] M. Schechter and N. Laflorencie, CondMat arXiv **0511304**, 1 (2005).

[74] S. Tabei, M. Gingras, Y.-J. Kao, P. Stasiak, and J.-Y. Fortin, CondMat arXiv **0608145**, 1 (2006).

[75] M. Schechter, P. C. E. Stamp, and N. Laflorencie, CondMat arXiv **0608622**, 1 (2006).

[76] J. Nikkel and B. Ellman, CondMat arXiv **0504269**, 1 (2005).

[77] J. Rodriguez *et al.*, Physica B **374**, 13 (2006).

[78] F. Pobell, *Matter and Methods at Low Temperatures* (Springer-Verlag, Berlin, 1992).

[79] N. O. Birge and S. R. Nagel, Phys. Rev. Lett. **54**, 2674 (1985).

[80] J. L. Devore, *Probability and Statistics for Engineering and teh Sciences* (Brooks/Cole Publishing Co., 1995).

[81] D. L. Martin, Phys. Rev. B **21**, 1980 (1980).

[82] F. Tanaka, J. Phys. C **13**, L951 (1980).

[83] D. Meschede, F. Steglich, W. Felsch, H. Maletta, and W. Zinn, Phys. Rev. Lett. **44**, 102 (1980).

[84] J. Souletie and R. Tournier, J. Low. Temp. Phys. **1**, 95 (1969).

[85] H. v. Löhneysen, Phys. Rev. B **22**, 273 (1980).

[86] G. Schehr, Phys. Rev. B **71**, 184204 (2005).

[87] D. L. Martin, Physical Review B **20**, 368 (1979).

[88] N. Vernier and G. Bellessa, Phys. Rev. Lett. **71**, 4063 (1993).

[89] M. Evangelisti, F. Luis, F. L. Mettes, R. Sessoli, and L. J. de Jongh, Phys. Rev. Lett. **95**, 227206 (2005).